

# 1        **A CRISPR/Cas9 genetically engineered organoid biobank reveals** 2                                    **essential host factors for coronaviruses**

3

4    Joep Beumer<sup>1,3</sup>, Maarten H. Geurts<sup>1,3</sup>, Mart M. Lamers<sup>2,3</sup>, Jens Puschhof<sup>1</sup>, Jingshu Zhang<sup>2</sup>, Jelte van der  
5    Vaart<sup>1</sup>, Anna Z. Mykytyn<sup>2</sup>, Tim I. Breugem<sup>2</sup>, Samra Riesebosch<sup>2</sup>, Debby Schipper<sup>2</sup>, Petra B. van den  
6    Doel<sup>2</sup>, Wim de Lau<sup>1</sup>, Cayetano Pleguezuelos-Manzano<sup>1</sup>, Georg Busslinger<sup>1</sup>, Bart L. Haagmans<sup>2,\*</sup> and  
7    Hans Clevers<sup>1,\*</sup>

8

9    <sup>1</sup>Oncode Institute, Hubrecht Institute, Royal Netherlands Academy of Arts and Sciences and University  
10    Medical Center, Utrecht, Netherlands.

11    <sup>2</sup> Viroscience Department, Erasmus Medical Center, Rotterdam, Netherlands.

12    <sup>3</sup> Co-first authors

13    \*Correspondence to: [h.clevers@hubrecht.eu](mailto:h.clevers@hubrecht.eu) and [b.haagmans@erasmusmc.nl](mailto:b.haagmans@erasmusmc.nl)

## 14    **Abstract**

15    **Rapid identification of host genes essential for virus replication may expedite the generation of**  
16    **therapeutic interventions. Genetic screens are often performed in transformed cell lines that poorly**  
17    **represent viral target cells in vivo, leading to discoveries that may not be translated to the clinic.**  
18    **Intestinal organoids (IOs) are increasingly used to model human disease and are amenable to genetic**  
19    **engineering. To discern which host factors are reliable anti-coronavirus therapeutic targets, we**  
20    **generate mutant clonal IOs for 19 host genes previously implicated in coronavirus biology. We verify**  
21    **ACE2 and DPP4 as entry receptors for SARS-CoV/SARS-CoV-2 and MERS-CoV respectively. SARS-CoV-**  
22    **2 replication in IOs does not require the endosomal Cathepsin B/L proteases, but specifically**  
23    **depends on the cell surface protease TMPRSS2. Other TMPRSS family members were not essential.**  
24    **The newly emerging coronavirus variant B.1.1.7, as well as SARS-CoV and MERS-CoV similarly**  
25    **depended on TMPRSS2. These findings underscore the relevance of non-transformed human models**  
26    **for coronavirus research, identify TMPRSS2 as an attractive pan-coronavirus therapeutic target, and**  
27    **demonstrate that an organoid knockout biobank is a valuable tool to investigate the biology of**  
28    **current and future emerging coronaviruses.**



62 compensate for the loss of TMPRSS2. Similarly, several new host factors have recently been found to  
63 play a role in the SARS-CoV-2 replication cycle, such as NRP1 and NDST1, but it is unknown whether  
64 these genes could be used as anti-SARS-CoV-2 drug targets<sup>12-14</sup>.

65 There may exist significant differences between individual transformed cell lines, and between  
66 transformed and non-transformed cells in viral entry pathways. Intestinal organoid (IO) culture  
67 systems are an attractive platform to study virus-host interactions as they are amenable to CRISPR-  
68 Cas9 mediated gene editing to directly identify host proteins utilized by the virus. Their self-renewing  
69 nature offers an additional advantage: biobanks of characterized mutant IO clones can be established,  
70 stored and shared. Here we establish a biobank of mutant IOs in genes implied in coronavirus biology  
71 and test their role in coronavirus replication to discern which host factors may represent anti-  
72 coronavirus therapeutic targets. This biobank can be used as a tool to rapidly identify which genes are  
73 essential for virus entry when novel SARS-CoV-2 variants or novel zoonotic (corona)viruses emerge.

## 74 **Results**

### 75 ***Transcriptomic analysis of human IOs and airway cultures reveal conserved expression of*** 76 ***coronavirus host factors***

77 Multiple host factors such as entry receptors and proteases are involved in viral replication cycles<sup>15</sup>.  
78 Since organoids closely resemble the physiology of human tissues, we used IOs to assess the function  
79 of individual host factors that have been implicated in the SARS-CoV-2 replication cycle, or of other  
80 coronaviruses. We and others have previously shown that SARS-CoV-2 can replicate in human IOs<sup>16-18</sup>,  
81 consistent with observations of gastrointestinal symptoms in COVID-19<sup>19,20</sup>. Intestinal organoids are  
82 readily amenable to genetic engineering by CRISPR-Cas9<sup>21</sup>, allowing to test the role of host genes in  
83 the replication of SARS-CoV-2. We reasoned that individual host factors that upon loss-of-function  
84 affect coronavirus replication, represent interesting drug targets for the treatment of COVID-19. As  
85 spike protein cleavage is an essential step for viral entry, we focused on the proteases TMPRSS2,  
86 TMPRSS3, TMPRSS4, TMPRSS11D, TMPRSS13, Cathepsin B (CTSB), Cathepsin L (CTSL) and Furin, that  
87 have previously been implicated in the entry of SARS-CoV-2 or other coronaviruses<sup>9,22,23</sup>. Besides  
88 proteases, we included the following (putative) entry or attachment factors: the protease DPP4 (MERS-  
89 CoV), peptidase ANPEP (human coronavirus 229E receptor<sup>24</sup>, C-type lectin CLEC2B<sup>25</sup>, structural protein  
90 Vimentin<sup>26</sup>, glycoprotein CEACAM1<sup>27</sup>, tetraspanin CD9<sup>28</sup>, C-type lectin receptor CD209 (DC-SIGN)<sup>29</sup>,  
91 VEGF co-receptor NRP1<sup>13,14</sup>, MAVS which indirectly senses cytoplasmic RNA<sup>30</sup>, heatshock protein  
92 HSPA5<sup>31</sup>, the sulfotransferase NDST1<sup>12</sup> and the RNA packaging protein ARC (upregulated upon SARS-  
93 CoV-2 infection<sup>17</sup>, Fig. S6E) as putative host factors involved in replication.



126 To unequivocally demonstrate that physiological levels of ACE2 are essential for SARS-CoV-2 entry into  
127 non-transformed human epithelial cells, we analyzed mutant ACE2 IOs for their ability to support SARS-  
128 CoV-2 replication. ACE2, located on the apical membrane of cells in wildtype IOs, was lost in mutant  
129 clones (Fig. 2C). ACE2-deficient IOs were fully resistant to SARS-CoV-2 infection (Fig. 3A). Indeed, we  
130 did not detect SARS-CoV-2 infected cells in ACE2-knockout organoids by immunofluorescence (Fig. 3B).  
131 Similarly, infection with SARS-CoV was abrogated in ACE2-knockout organoids (Fig. S5A). We  
132 concluded that ACE2 is the obligate entry receptor for SARS-CoV-2 and SARS-CoV, and that no  
133 redundancy exists with other surface proteins in intestinal epithelial cells. The presence of infected  
134 cells that appear ACE2-negative, implies either that surface receptors are downregulated upon  
135 infection or that low levels of ACE2 proteins suffice. To confirm that viral entry occurs through the  
136 apical membrane - where ACE2 is located - we attempted viral infection following our standard  
137 approach in which organoids are mechanically disrupted, and using intact organoids where only the  
138 basolateral surface is exposed. We could observe viral replication only in disrupted organoids,  
139 supporting an obligate apical entry route for SARS-CoV-2 (Fig. S5B).

#### 140 ***MERS-CoV infects human IOs in a DPP4-dependent manner***

141 DPP4 has been shown to be the entry receptor for MERS-CoV by spike co-immunoprecipitation and  
142 overexpression in non-susceptible cells<sup>6</sup>. We first established that human IOs allow replication of  
143 MERS-CoV (Fig. S6A). In contrast to SARS-CoV-2, MERS-CoV caused extensive cell death, killing the  
144 majority of cells in organoids within 48 hours of infection (Fig. S6A). Transcriptomic analysis revealed  
145 a strong upregulation of heat shock- and unfolded protein responses, while interferons were  
146 effectively repressed (Fig. S6B-E, Tables S3-4). This was consistent with previous reports that MERS-  
147 CoV encodes an extensive set of proteins that inhibit interferon responses<sup>38</sup>. We generated loss-of-  
148 function DPP4-mutant IO clones (Table S2). An infection assay on two of these clones revealed that  
149 MERS-CoV replication was fully blocked, while SARS-CoV-2 replicated in the DPP4-mutant organoids at  
150 control levels (Fig. 3C). Immunofluorescence confirmed loss of DPP4 protein in mutant clones as well  
151 as the successful replication of SARS-CoV-2 -but not of MERS-CoV- in these organoids (Fig. 3D).  
152 Conversely, MERS-CoV propagated in ACE2-deficient organoids at control levels (Fig. S5A).

#### 153 ***Loss-of-function screen of host proteases reveals essential role in viral replication for TMPRSS2 but*** 154 ***not other TMPRSS family members or Cathepsins***

155 We next analyzed all IO lines that were mutant in proteases for their ability to support SARS-CoV-2  
156 replication. Knockout of TMPRSS2 effectively blocked viral replication, while mutation of any of other  
157 TMPRSS-genes had no effect (Fig. 4A-B). Complete depletion of TMPRSS2 protein was confirmed using

158 immunohistochemistry (Fig. S7A). These experiments were performed using a VeroE6-propagated  
159 stock and recent work has pointed out that propagation on VeroE6 cells can lead to culture adaptive  
160 mutations in the multibasic cleavage site<sup>39-43</sup>. The VeroE6 stock used in this study was deep-  
161 sequenced<sup>39</sup> and was 64.2% wild-type in the RRAR (spike positions 682-685) multibasic cleavage site.  
162 We detected another mutation adjacent to the multibasic cleavage site (S686G) at a frequency of  
163 45.4%. Viruses with multibasic cleavage site cleavage site mutations, including S686G, were shown to  
164 slightly increase cathepsin usage by ~20%<sup>39</sup>, indicating that the majority of these viruses still used  
165 serine protease-mediated entry.

166 We have previously shown that propagation in TMPRSS2-expressing Calu-3 cells prevents culture  
167 adaptation. Using this Calu-3 stock that was completely non-adapted<sup>39</sup>, we confirmed the dependency  
168 of SARS-CoV-2 on TMPRSS2 (and ACE2) (Fig. 4C). Immunofluorescence of TMPRSS2-deficient organoids  
169 showed absence of viral spread (Fig. 4D). This implied that TMPRSS2 is the main proteolytic activator  
170 of the SARS-CoV-2 spike protein. In contrast to knockout screens in VeroE6 cells that showed that the  
171 endocytic pathway protease Cathepsin L was essential for SARS-CoV-2 entry<sup>9</sup>, SARS-CoV-2 replicated -  
172 if anything- more efficiently in Cathepsin L-mutant than in wildtype organoids (Fig. 4A-B). Efficient  
173 depletion of Cathepsin L was supported using western blot analysis (Fig. S7B). We confirmed the  
174 obligate role of TMPRSS2 for SARS-CoV-2 replication in IOs derived from a different donor and from  
175 another segment (duodenum) of the human intestine (Fig. 4E).

176 Since we observed differential expression of multiple proteases - including upregulation of cathepsins  
177 - in differentiated organoids, we additionally assessed TMPRSS2-dependency in differentiated  
178 intestinal cells (Fig. S7C). After 5 days of differentiation, both wildtype and TMPRSS2-mutant organoids  
179 were infected with SARS-CoV-2. SARS-CoV-2 replicated efficiently in differentiated organoids, as we  
180 reported previously<sup>17</sup>. Viral replication was greatly diminished in TMPRSS2-deficient organoids,  
181 suggesting dependency on this protease across different intestinal cell types (Fig. S7D)

182 To assess redundancy in single TMPRSS- or cathepsin-mutant organoids, we additionally generated  
183 organoids mutant for both CTSL/CTSB, or TMPRSS2/4, the most abundantly expressed cathepsins and  
184 serine proteases in the intestinal epithelium. Previous work implied a role for TMPRSS4 in viral entry  
185 in the intestinal epithelium<sup>33</sup>. We did not observe reduced replication when both cathepsins were lost.  
186 Moreover, TMPRSS4 knock-out in a TMPRSS2-mutant background did not further decrease infectivity  
187 (Fig. S7E). In line with this, the broad serine protease inhibitor camostat did not affect replication in  
188 TMPRSS2-deficient IOs (Fig. S7F). We concluded that the cathepsins and TMPRSS4 do not play a role  
189 in viral entry in the intestinal epithelium.

190 To confirm that the endocytic pathway is dispensable for viral entry, we treated IOs with 1) the  
191 endosomal pathway inhibitor chloroquine, the cathepsin protease inhibitor E64D, or the broad serine  
192 protease inhibitor camostat. These drugs were well-tolerated with no growth impairment at the  
193 concentrations used (Fig. S8A-B). As published previously, chloroquine was effective in VeroE6 cells  
194 (Fig. S8C)<sup>7</sup>. While camostat effectively inhibited viral replication, chloroquine and E64D did not affect  
195 replication in IOs (Fig. 4F). E64D-treated organoids displayed a trend towards more efficient viral  
196 replication (Fig. 4F), consistent with observations in the Cathepsin L-mutant organoids (Fig. 4A-B). We  
197 concluded that Cathepsin-mediated entry through the endosomal route may be the central port of  
198 viral entry in cell lines, but not in IOs, in which SARS-CoV-2 enters through the activity of TMPRSS2 (Fig  
199 4A-B). These observations may also explain why (hydro)-chloroquine has emerged from cell line  
200 studies but has proven ineffective in the clinic.

### 201 ***Redundancy for non-protease host factors in viral replication***

202 We further tested IOs mutant in a range of non-protease host factors to assess their role in coronavirus  
203 replication, of which some have already been linked to the SARS-CoV-2 replication cycle. NRP1 recently  
204 attracted attention as a novel co-receptor for SARS-CoV-2 in two separate studies that used HeLa,  
205 HEK293T and the colorectal cancer cell line Caco-2<sup>13,14</sup>. These findings were substantiated by x-ray  
206 crystallography data supporting binding of the viral spike protein to NRP1 SARS-CoV-2 infection was  
207 significantly inhibited by NRP1-blocking antibodies<sup>13,14</sup>. Additionally, CD209 was recently identified as  
208 potential SARS-CoV-2 receptor, and facilitated viral entry in HEK-293 cells when overexpressed<sup>36</sup>. A  
209 recent study found that SARS-CoV-2 can bind heparan sulfate on the cell surface through its spike  
210 protein. When enzymes involved in the sulfation of heparan sulfate, including NDST1, were knocked  
211 out in Hep3B cells, viral replication was almost entirely abolished<sup>12</sup>. None of these, nor the additional  
212 host factors we assessed, significantly impacted on viral replication when mutated in IOs (Fig. 5A, Fig.  
213 S9). We conclude that all of these proteins would therefore not be viable drug targets for the treatment  
214 of COVID-19 (Fig. 5B). Further studies may assess whether loss of these factors influence the cellular  
215 response to coronaviruses in any other way than replication efficiency.

### 216 ***TMPRSS2-dependency in SARS-CoV-2 B.1.1.7, SARS-CoV and MERS-CoV***

217 The mutant host factor KO biobank can readily be employed when new coronaviruses or viral strains  
218 appear, to assess the dependency on host factors and identify druggable targets. We first tested  
219 whether the same TMPRSS2-dependency exists for the other two coronaviruses. SARS-CoV replication  
220 was strongly diminished upon TMPRSS2 loss, while MERS-CoV replication was reduced more modestly  
221 (Fig. 6A). The latter potential redundancy may be explained by the presence of two functional

222 multibasic cleavage sites in the MERS-CoV spike, whereas SARS-CoV-2 and SARS-CoV possess one and  
223 none, respectively<sup>22</sup>. Both viruses could replicate in the absence of Cathepsin L, suggesting that  
224 coronaviruses generally do not use the endosomal entry route in primary epithelial cells as present in  
225 organoids (Fig. 6A).

226 Recently, a novel SARS-CoV-2 variant (clade B.1.1.7 or British variant) emerged and is rapidly replacing  
227 endemic viruses globally. Epidemiological data suggest that this variant is 1.35-2 fold more  
228 transmissible than the ancestral lineage and is associated with higher viral loads<sup>44-46</sup>. Interestingly, this  
229 variant contains a mutation (P681H) directly N-terminal from the RRAR multibasic cleavage site that  
230 adds another basic residue to the multibasic cleavage site, creating an HRRAR motif. A similar mutation  
231 (P681R) was detected in the Indian variant (clade B.1.617). As the multibasic cleavage site facilitates  
232 serine protease-mediated entry<sup>11</sup>, mutations in or near this site may alter protease usage for S2'  
233 cleavage, which directly triggers fusion and entry. We found that the British variant replicated  
234 efficiently in wildtype and cathepsin mutant organoids, but not in TMPRSS2-deficient cells (Fig. 4E),  
235 indicating that the British variant did not broaden its protease usage. These experiments provide a  
236 proof-of-concept on how emerging viral strains could be screened against mutant IOs.

## 237 **Discussion**

238 The current COVID-19 pandemic has exposed weaknesses in our preparedness for coronavirus  
239 pandemics. No effective coronavirus antivirals are approved for use in humans and all completed large-  
240 scale COVID-19 drug trials have failed to show efficacy to this date, including (hydroxy)chloroquine and  
241 remdesivir<sup>8,47</sup>. The disappointing clinical effects of (hydroxy)chloroquine in humans in particular  
242 highlights gaps in the understanding of fundamental coronavirus biology. (Hydroxy)chloroquine, an  
243 inhibitor of the endosomal acidification was identified as a potent inhibitor of SARS-CoV<sup>48</sup> and SARS-  
244 CoV-2<sup>7</sup> viral entry in cell line-based assay, confirmed here. In agreement with this, recent whole  
245 genome CRISPR/Cas9 genetic screens in transformed cell lines again suggested that endosomal entry  
246 factors, such as cathepsin L, are crucial for SARS-CoV-2 entry<sup>9,49,50</sup>.

247 Here, we use human intestinal organoids as a non-transformed model to study genes implicated in  
248 coronavirus biology. We have chosen to use only IOs since it is currently not possible to efficiently  
249 genetically engineer airway organoids due to limited clonal outgrowth of these cells. Nevertheless, IOs  
250 express the majority of host factors assessed, including proteases, to a similar level as the airways (Fig.  
251 1). We confirmed that in this model ACE2 is the obligate entry receptor for SARS-CoV-2 and SARS-CoV,  
252 while DPP4 is the entry receptor for MERS-CoV, indicating that accessory receptors may not play crucial  
253 roles for these viruses. Indeed, knockout of NRP1, recently proposed as a SARS-CoV-2 (co-)receptor in



254 HeLa and Caco-2 cells, did not affect SARS-CoV-2 entry<sup>13,14</sup>. Furthermore, we demonstrate that  
255 Cathepsin L and B are not involved in SARS-CoV-2 entry in IOs. In accordance with this, a cathepsin  
256 inhibitor (E64D) and chloroquine did not inhibit SARS-CoV-2 in these IOs, while the serine protease  
257 inhibitor Camostat effectively blocked viral propagation. A similar anti-SARS-CoV-2 effect of camostat  
258 was observed in organoid-derived airway cells<sup>11</sup>. The broad activity of Camostat does not allow to  
259 pinpoint which serine protease mediates entry.

260 TMPRSS2-deficiency in IOs strongly decreased SARS-CoV-2 replication and spread, indicating that  
261 TMPRSS2 is the main priming protease. Other related TMPRSS genes have previously also been linked  
262 to SARS-CoV-2 replication, including TMPRSS4 in the intestine<sup>33</sup>. Overexpression of TMPRSS11D and  
263 TMPRSS13 promoted viral entry into the hamster kidney cell line BHK-21<sup>51</sup>, while TMPRSS4  
264 overexpression facilitated viral entry in HEK293 cells<sup>33</sup>. Like TMPRSS2, TMPRSS4 is highly expressed in  
265 intestinal tissue and IOs, yet TMPRSS4 does not appear to rescue loss of TMPRSS2. This discrepancy  
266 with previous work may reflect the fact that our study relies on physiological expression of these  
267 proteases, rather than on overexpression. Importantly, intestinal organoids express similar TMPRSS  
268 family members compared to airway tissue, including high levels of TMPRSS2, TMPRSS3, TMPRSS4 and  
269 TMPRSS13. Only the TMPRSS-11A and -11D are relatively enriched in airway- versus intestinal  
270 epithelium<sup>52</sup>. Although we cannot exclude the possibility that these TMPRSS family members function  
271 in activation of SARS-CoV-2 spike in the airways, their expression levels are much lower than that of  
272 TMPRSS2 in airway organoids (Fig. 1A) and lung tissue<sup>52</sup>.

273 Altogether, these findings indicate that multiple TMPRSS genes may be able to mediate entry when  
274 overexpressed, but -at physiological levels in IOs- only TMPRSS2 plays an essential role, which may  
275 inspire the development of high-specificity TMPRSS2 inhibitors. The high TMPRSS-2 dependency of  
276 SARS-CoV (this study) indicates that such inhibitors may well be effective against future SARS-like  
277 coronavirus pandemics. The observation that TMPRSS2-null mice do not display a visible phenotype<sup>53</sup>  
278 implies that such inhibitors may be well-tolerated. Our findings match with observations that SARS-  
279 CoV and to a lesser extent MERS-CoV replication and dissemination was reduced in TMPRSS2-deficient  
280 mice<sup>54</sup>.

281 In conclusion, our findings underscore the relevance of non-transformed human models for  
282 (corona)virus research and identify TMPRSS2 as an attractive therapeutic target in contrast to many  
283 other genes (e.g. cathepsin L, cathepsin B, NRP1, NDST1 etc) that -as deduced from our observations-  
284 unlikely to be of clinical value. Future emerging viruses could be readily screened against our IO host  
285 factor knockout biobank to rapidly identify therapeutic targets.

286 **Acknowledgements**

287 We thank Single Cell Discoveries for RNA library preparation, and R. van der Linden and S. van Elst for  
288 help with FACS sorting. We thank E. Eenjes and R. Rottier for providing human lung material.

289 **Author contributions**

290 J.B., M.H.G. and M.M.L. designed the study and performed the experiments. J.P. and J.V. analyzed  
291 RNA-sequencing data. B.H. and H.C. supervised the study.

292 **Declaration of interest**

293 H.C. is inventor on several patents related to organoid technology; his full disclosure is given at  
294 <https://www.uu.nl/staff/JCClevers/>.

295 **Figure legends**

296 **Figure 1 Expression levels of host genes potentially involved in SARS-CoV-2 biology in lung and**  
297 **intestinal organoids and tissue**

298 a) Graphs depicting the transcript counts (logarithmic scale) determined by RNA sequencing of host  
299 factors and proteases in organoids derived from different parts of the airway and intestine. Airway  
300 organoids (trachea, bronchus and bronchiole) were differentiated as 2D ALI-cultures.

301 b) t-SNE maps and violin plots displaying expression of host factors in the human intestinal organoid  
302 cell and human intestinal tissue atlases (in vivo atlas derived from<sup>32</sup>. Bars in t-SNE maps display color-  
303 coded normalized unique transcript expression (logarithmic scale).

304 **Figure 2 Generation of a coronavirus host gene knockout biobank**

305 a) Overview of the workflow of generation of gene knockouts.

306 b) Overview of the number of clones that were amplified and biobanked in this study.

307 c) Immunofluorescent staining of WT and ACE2 KO organoids. ACE2 locates to the apical membrane  
308 and is absent in mutant organoids. Scale bars are 50  $\mu\text{m}$ . Contrast was enhanced in unzoomed images  
309 for visualization purposes.

310 **Figure 3 ACE2 and DPP4 are the obligate entry receptors for SARS-CoV-2 and MERS-CoV respectively**

311 a) qPCR analysis targeting the E gene to quantify viral replication of wildtype (WT) and ACE2 knockout  
312 (KO) organoids. Error bars represent SEM. Each data point represents the mean of 3 replicates.

313 b) Immunofluorescent staining of WT and ACE2 KO organoids, infected with SARS-CoV-2 visualized by  
314 nucleocapsid protein and dsRNA. ACE2 locates to the apical membrane and is absent in mutant  
315 organoids.

316 c) qPCR analysis targeting the E gene (SARS-CoV-2) or upE region (MERS-CoV) to quantify viral  
317 replication in WT and DPP4 KO organoids. Each data point represents the mean of 3 replicates.

318 d) Immunofluorescent staining of MERS-CoV (visualized by dsRNA) and SARS-CoV-2 (visualized by  
319 nucleocapsid protein) infected organoids. DPP4 locates to the apical membrane and is absent in  
320 mutant organoids. Scale bars are 50  $\mu$ m.

321 **Figure 4 Loss-of-function screen of host proteases reveals essential role for TMPRSS2 but not**  
322 **Cathepsins in viral replication**

323 a) Violin plot displaying the Log<sub>10</sub> ratio between the viral titer at 48 hours compared to 2 hours post  
324 infection (p.i.) quantified by qPCR targeting the E gene. The dotted line indicates a fold change of 1.  
325 Dotted lines within the violins indicate the median and quartiles. Data from replication curves in Fig.  
326 3A and 3C is included. N  $\geq$  3.

327 b) qPCR analysis targeting the E gene to quantify viral replication of wildtype organoids and cells  
328 harboring a loss-of-function of a single host factor. Error bars represent SEM. Each data point  
329 represents the mean of 3 replicates.

330 c) Violin plot displaying the Log<sub>10</sub> ratio between the viral titer at 48 hours compared to 2 hours post  
331 infection (p.i.) quantified by qPCR targeting the E gene in organoids infected with SARS-CoV-2  
332 propagated on Calu-3 cells. The dotted line indicates a fold change of 1. Dotted lines within the violins  
333 indicate the median and quartiles. N  $\geq$  3.

334 d) Immunofluorescent staining of SARS-CoV-2 infected WT and CTSL and TMPRSS2 KO organoids. Virus  
335 is visualized by nucleocapsid protein. TMPRSS2 KO organoids do not facilitate viral infection, although  
336 very rare, infected cells can be observed. CTSL KO organoids display abundant viral infection. Scale bars  
337 are 50  $\mu$ m.

338 e) Violin plot displaying the Log<sub>10</sub> ratio between the viral titer at 48 hours compared to 2 hours post  
339 infection (p.i.) quantified by qPCR targeting the E gene in organoids of the human duodenum. The

340 dotted line indicates a fold change of 1. Dotted lines within the violins indicate the median and  
341 quartiles.  $N \geq 3$ .

342 f) qPCR analysis targeting the E gene to quantify viral replication of organoids treated with the serine  
343 protease inhibitor Camostat, chloroquine or cysteine protease inhibitor E64D. Error bars represent  
344 SEM. Each data point represents the mean of 3 replicates.

345  $P < 0.05$  \*;  $P < 0.01$  \*\* ;  $P < 0.001$  \*\*\* ;  $P < 0.0001$  \*\*\*\*.

#### 346 **Figure 5 Replication of SARS-CoV-2 in additional proposed host factors**

347 a) ) Violin plot displaying the Log10 ratio between the viral titer at 48 hours compared to 2 hours post  
348 infection (p.i.) quantified by qPCR targeting the E gene in wildtype organoids and cells harboring a loss-  
349 of-function of a single host factor. Graphs display the ratio between viral titer at 48 hours compared  
350 to 2 hours post infection (p.i.). The dotted line indicates a fold change of 1. Dotted lines within the  
351 violins indicate the median and quartiles.  $N \geq 2$ . The WT data is redisplayed from Fig. 4A.

352 b) Model of host entry receptors and proteases involved in the entry of SARS-CoV-2. Essential and non-  
353 essential host factors based on the phenotypes in IO mutants are marked

#### 354 **Figure 6 Host protease dependency in the SARS-CoV-2 strain B.1.1.7 and other coronaviruses**

355 a) ) Violin plot displaying the Log10 ratio between the viral titer at 48 hours compared to 2 hours post  
356 infection (p.i.) quantified by qPCR targeting the the N gene (SARS-CoV) or upE region (MERS-CoV) to  
357 measure viral replication in WT and TMPRSS2 KO organoids. DPP4 and ACE2 data include replication  
358 curves in Fig. 3C and S4A. The dotted line indicates a fold change of 1. Dotted lines within the violins  
359 indicate the median and quartiles.  $N \geq 3$ .

360 b) Violin plot displaying the Log10 ratio between the viral titer at 48 hours compared to 2 hours post  
361 infection (p.i.) quantified by qPCR targeting the E gene to measure viral replication of the SARS-CoV-2  
362 B.1.1.7 strain in intestinal organoid cells harboring a loss-of-function mutation in the TMPRSS2 and  
363 CTSL proteases, or ACE2. The dotted line indicates a fold change of 1. Dotted lines within the violins  
364 indicate the median and quartiles.  $N \geq 3$ .

365  $P < 0.05$  \*;  $P < 0.01$  \*\* ;  $P < 0.001$  \*\*\* ;  $P < 0.0001$  \*\*\*\*.

#### 366 **Supplementary figure 1 Bulk and single cell RNA sequencing reveals intestinal expression of host** 367 **proteases involved in viral entry**

368 a) Heatmaps depicting expression of host genes (top) and proteases (bottom) in intestinal, nose and  
369 airway organoids. Nose organoids were cultured in expansion (EM) or differentiation (DM) medium.  
370 Colored bar represents Z-score of log<sub>2</sub> transformed values.

371 b) t-SNE maps displaying a newly generated human organoid single cell RNA sequencing atlas (left),  
372 and a dataset reanalyzed from<sup>32</sup> (right). Colors indicate different cell types.

373 c) t-SNE maps displaying the human organoid single cell sequencing atlas. Color codes indicate cells  
374 derived from expansion or differentiation medium.

375 d) t-SNE maps and violin plots displaying expression of host factors in the human intestinal organoid  
376 cell atlas. Bars in t-SNE maps display color-coded normalized unique transcript expression (logarithmic  
377 scale).

378 e) t-SNE maps and violin plots displaying expression of host factors in the human intestinal tissue atlas.  
379 Bars in t-SNE maps display color-coded normalized unique transcript expression (logarithmic scale).

380

### 381 **Supplementary figure 2 Generation of a host factor loss-of-function organoid biobank**

382 Overview of the genetic alterations causing frameshifts in the different host factors. Green boxes  
383 indicate PAM sequence, red dashes or bases indicate respectively deletions and insertions.

### 384 **Supplementary figure 3 Organoid genotyping by sanger sequencing and *in silico* ICE analysis.**

385 Sanger traces and subsequent *in silico* sanger deconvolution by ICE v2 for the first clone of ACE2,  
386 TMPRS2, DDP4 and CTSL indicating out-of-frame indel induction at the target site. Green boxes  
387 indicate PAM sequence.

### 388 **Supplementary figure 4 SARS-CoV-2 infected cells contain varying degrees of membranous ACE2 389 protein**

390 Immunofluorescent staining of SARS-CoV-2 infected organoids. Virus is visualized by dsRNA. Some  
391 infected cells are devoid of visible ACE2 on the outer membrane. Scale bars are 50 μm.

### 392 **Supplementary figure 5 SARS-CoV but not MERS-CoV replication depends on ACE2**

393 a) qPCR analysis targeting the N gene (SARS-CoV) or upE region (MERS-CoV) to quantify viral replication  
394 in WT and ACE2 KO organoids. Error bars represent SEM. Each data point represents the mean of 3  
395 replicates.

396 b) qPCR analysis targeting the E gene to quantify viral replication of the SARS-CoV-2 in mechanically  
397 disrupted or intact organoids, where virus can only access the basolateral side. Graphs display the ratio  
398 between viral titer at 48 hours compared to 2 hours post infection (p.i.). Each data point represents  
399 the mean of 3 replicates. Error bars represent SEM.

#### 400 **Supplementary figure 6 Establishment of MERS infection model in human intestinal organoids**

401 a) Immunofluorescent staining of organoids 48 hours after MERS-CoV infection. Virus is visualized by  
402 staining for the spike protein. The majority of the infected organoids display massive cell death. Scale  
403 bars are 50  $\mu$ m.

404 b) Graphs depicting the transcript counts determined by RNA sequencing of different genes upon  
405 MERS-CoV infection. Different numbers indicate timepoints (hours) after infection

406 c) Graph depicting the transcript counts mapping to human and MERS genomes in MERS-CoV infected  
407 organoids. MERS reads increase over time, but drop again at 48 hours potentially due to cell death of  
408 infected cells. For all other analyses, MERS reads were removed from analyses for normalization  
409 purposes.

410 d) Go term enrichment analysis for biological processes of the 60 most significantly upregulated genes  
411 upon MERS-CoV infection in organoids.

412 e) Heatmap depicting the expression profile of the 25 genes with strongest upregulation upon SARS-  
413 CoV-2 infection<sup>17</sup>; right heatmaps) and the same genes upon MERS-CoV infection (left heatmaps). The  
414 top heatmaps show the most prominently upregulated genes after 60 hours of SARS-CoV-2 infection,  
415 the lower heatmaps after 24 hours. In contrast to SARS-CoV-2, MERS-CoV does not induce expression  
416 of ISGs. Colored bar represent Z-score of log<sub>2</sub> transformed values.

#### 417 **Supplementary figure 7 Lack of redundancy in cathepsins and serine proteases in viral entry**

418 a) Immunohistochemical staining of TMPRSS2 in wildtype and TMPRSS2-knock out (KO) organoids.  
419 TMPRSS2 locates mostly to the apical membrane in wildtype cells, and is absent in mutant organoids.  
420 Scale bars are 50  $\mu$ m.

421 b) Western blotting for CTSL and Integrin B4 (ITGB4, loading control) in wildtype, TMPRSS2- and CTSL-  
422 KO organoids. CTSL protein is completely lost in corresponding mutant organoids

423 c) Brightfield images of expanding and 5-day differentiated organoids that were infected with SARS-  
424 CoV-2. Scale bars are 400  $\mu$ m.

425 d) Graph displaying the ratio between the viral titer at 48 hours compared to 2 hours post infection  
426 (p.i.) quantified by qPCR targeting the E gene to measure viral replication of SARS-CoV-2 in expanding  
427 and 5-day differentiated intestinal organoid cells harboring a loss-of-function mutation in the TMPRSS2  
428 gene. Error bars represent SEM. N=2.

429 e) qPCR analysis targeting the E gene to quantify viral replication of the SARS-CoV-2 in organoids  
430 harboring different single and double mutants in host proteases. Graphs display the ratio between  
431 viral titer at 48 hours compared to 2 hours post infection (p.i.). Error bars represent SEM. The dotted  
432 line indicates a fold change of 1. N=2.

433 f) qPCR analysis targeting the E gene to quantify viral replication of the SARS-CoV-2 in TMPRSS2-  
434 deficient organoids treated with the broad serine protease inhibitor Camostat. Graphs display the ratio  
435 between viral titer at 48 hours compared to 2 hours post infection (p.i.). Error bars represent SEM.  
436 N=2.

437 **Supplementary figure 8 Inhibition of serine proteases but not chloroquine inhibits viral replication**  
438 **in organoids**

439 a) Brightfield images of organoids treated for 48 hours with serine protease inhibitor Camostat,  
440 chloroquine or cysteine protease inhibitor E64D.

441 b) Violin plot of average sizes in organoids from Fig. 6E. The diameter was measured in at least n=50  
442 organoids per treatment. Organoid size was not significantly changed in any of the treatments,  
443 indicating similar growth. Dotted lines within the violins indicate the median and quartiles.

444 c) Quantification of viral entry in Vero E6 cells upon treatment with chloroquine using immunostaining  
445 8 hours after infection. Error bars represent SEM.

446 **Supplementary figure 9 SARS-CoV-2 replication in Furin- en ARC-mutant IOs**

447 Graph displaying the ratio between the viral titer at 48 hours compared to 2 hours post infection (p.i.)  
448 quantified by qPCR targeting the E gene to measure viral replication of SARS-CoV-2 in wildtype, and

449 ARC- and Furin- mutant organoids. Experiment was performed with n=1 biological replicate. The WT  
450 data is redisplayed from Fig. 4A.

451 **Supplementary table 1 Normalized transcript counts in intestinal and airway organoids**

452 Table shows normalized transcript counts determined by RNA sequencing of duplicate organoids from  
453 the respective regions, and intestinal organoids infected with SARS-CoV-2. The intestinal organoid  
454 dataset was obtained from<sup>17</sup>.

455 **Supplementary table 2 Overview of genetically modified organoids generated in this study**

456 **Supplementary table 3 Normalized transcript counts in MERS-CoV infected organoids**

457 Table shows normalized transcript counts determined by RNA sequencing of a duplicate control  
458 treatment (NC), and 16, 24 and 48 hours after MERS-CoV infection.

459 **Supplementary table 4 Differentially regulated genes upon MERS-CoV infection in organoids**

460 Fold change in gene expression versus control after 48 hours of MERS-CoV infection.

461 **Supplementary table 5 Oligos used in this study as gRNAs and sequencing primers**

462 **Methods**

463 **Cell culture of human intestinal organoids and human airway**

464 Human small intestinal tissue was obtained from the UMC Utrecht with informed consent of the  
465 patient. The patient was operated for a colorectal tumor, and a sample from non-transformed, normal  
466 mucosa was taken for this study. The study was approved by the UMC Utrecht (Utrecht, The  
467 Netherlands) ethical committee and was in accordance with the Declaration of Helsinki and according  
468 to Dutch law. This study is compliant with all relevant ethical regulations regarding research involving  
469 human participants.

470 Nasal inferior turbinate brushes were obtained from the Hadassah Medical Center, Jerusalem, with  
471 informed consent of the patient. Patients were diagnosed with primary ciliary dyskinesia, and tissue  
472 was obtained from healthy donors as a comparison. Healthy material was used for the RNA sequencing  
473 in this work. The study was approved by the ethical committee and was in accordance with the  
474 Declaration of Helsinki and according to Israeli law under IRB approval number 075-16 HMO. This study  
475 is compliant with all relevant ethical regulations regarding research involving human participants.



476 Adult lung tissue was obtained from residual, tumor-free, material obtained at lung resection surgery  
477 for lung cancer. The Medical Ethical Committee of the Erasmus MC Rotterdam granted permission for  
478 this study (METC 2012-512).

479 Human small intestinal cells were isolated, processed and cultured as described previously<sup>55,56</sup>. Wnt  
480 surrogate was used (0,15nM, U-Protein Express) instead of Wnt conditioned media. Differentiation of  
481 intestinal organoids was achieved as described previously<sup>56</sup>.

482 Nose tissue was dissociated and cultured as described previously<sup>57</sup>. Differentiation towards ciliated  
483 cells was performed by activating BMP signaling and inhibiting Notch signaling for 10 days (Van der  
484 Vaart et al., under review)

485 Isolation of human bronchial airway stem cells was performed using a protocol similar to Sachs and  
486 colleagues<sup>57</sup>. Small airway stem cells were isolated from distal human lung parenchyma as described  
487 before<sup>57</sup>. Tracheal stem cells were collected from tracheal aspirates of intubated preterm infants (28  
488 weeks gestational age). Organoids were cultured as described before<sup>57</sup>. To obtain differentiated  
489 organoid-derived cultures, organoids were dissociated into single cells using TrypLE express (Gibco;  
490 #12604013). Cells were seeded on Transwell membranes (Corning) coated with rat tail collagen type I  
491 (Fisher Scientific). Single cells were seeded in AO growth medium : complete base medium (CBM;  
492 Stemcell Pneumacult-ALI; #05001) at a 1:1 ratio. After 2-4 days, confluent monolayers were cultured  
493 at air-liquid interphase in CBM. Medium was changed every 5 days for 8 weeks.

#### 494 **Transfection of organoids for CRISPR-Cas9 experiments**

495 sgRNAs targeting loci of interest were cloned into a SpCas9-EGFP vector (addgene plasmid #48138)  
496 using a protocol described before<sup>58</sup>. sgRNAs were designed using WTSI website  
497 (<https://www.sanger.ac.uk/htgt/wge/>). A full list of gRNAs and primers to generate SpCas9-EGFP  
498 expressing plasmids can be found in supplementary table 5. To generate homozygous frameshift  
499 mutations in genes of interest, organoids were transfected with SpCas9-EGFP containing the locus-  
500 specific sgRNA. Transient transfection using a NEPA21 electroporator was performed as described  
501 before<sup>59</sup>. 3-7 days after transfection, organoids were dissociated using TrypLE (TrypLE Express; Life  
502 Technologies) and sorted on a FACS-ARIA (BD Biosciences) for GFP positivity. After sorting, Rho kinase  
503 inhibitor (Y-27632 dihydrochloride; 10µM, Abmole) was added for 1 week to support single cell  
504 outgrowth.

#### 505 **Generation of stable genetically modified organoid lines**

506 To generate clonal organoid lines with genotypes of preference, organoids were picked 2 weeks after  
507 sorting. Manually picked organoids were dissociated using TrypLE (TrypLE Express; Life Technologies)  
508 and plated in BME in pre-warmed cell culture plates. After two weeks, single cells grew into organoids  
509 and were split again to verify actively dividing stem cells. After the second split, 20 $\mu$ L of organoid-BME  
510 suspension was directly taken from the plate and DNA was extracted from the organoids using the  
511 Zymogen Quick-DNA microprep kit according to protocol. Regions around sgRNA target sites were  
512 amplified using Q5 high fidelity polymerase (NEB) according to manufacturer's protocol. CRISPR/Cas9-  
513 mediated indel formation was confirmed by sanger sequencing of these amplicons (Macrogen).  
514 Subsequently, sanger trace deconvolution was performed with the use of ICE v2 CRISPR analysis tool  
515 (synthego website) to call clonal organoid lines with homozygous frameshift mutations at the target  
516 site. Knockout clones were further expanded for viral infection experiments. Primers used for  
517 amplification and sanger sequencing can be found in supplementary table 5. For the generation of  
518 TMPRSS2/TMPRSS4 double mutants, TMPRSS4 was knocked out in TMPRSS2-clone 9. For the  
519 generation of CTSL/CTSB double mutants CTSL was knocked out in CTSB clone 3.

## 520 **Viruses and cell lines**

521 Vero and VeroE6 cells were maintained in Dulbecco's modified Eagle's medium (DMEM, Gibco)  
522 supplemented with 10% fetal calf serum (FCS), HEPES, sodium bicarbonate, penicillin (100 IU/mL) and  
523 streptomycin (100 IU/mL) at 37°C in a humidified CO<sub>2</sub> incubator. Calu-3 cells were maintained in Opti-  
524 MEM I (1X) + GlutaMAX (Gibco)(Gibco) supplemented with 10% FCS, penicillin (100 IU/mL) and  
525 streptomycin (100 IU/mL) at 37°C in a humidified CO<sub>2</sub> incubator. SARS-CoV (isolate HKU 39849,  
526 genbank accession no. AY278491), SARS-CoV-2 (isolate Bavpat-1; European Virus Archive Global  
527 #026V-03883; kindly provided by Dr. C. Drosten) were propagated on VeroE6 cells in Opti-MEM I (1X)  
528 + GlutaMAX (Gibco), supplemented with penicillin (100 IU/mL) and streptomycin (100 IU/mL) at 37°C  
529 in a humidified CO<sub>2</sub> incubator. MERS-CoV (isolate EMC, genbank accession no. NC019843) was  
530 propagated on Vero cells in the same medium. Non-adapted SARS-CoV-2 Bavpat-1 and B.1.1.7  
531 (genbank accession no. MW947280) were propagated in Calu-3 cells as described before<sup>39</sup>. Stocks were  
532 produced by infecting cells at a multiplicity of infection (MOI) of 0.01 and incubating the cells for 72  
533 hours. The culture supernatant was cleared by centrifugation and stored in aliquots at -80°C. Stock  
534 titers were determined by preparing 10-fold serial dilutions in Opti-MEM I (1X) + GlutaMAX. Aliquots  
535 of each dilution were added to monolayers of 2 × 10<sup>4</sup> VeroE6 (for SARS-CoV and SARS-CoV-2) or Vero  
536 cells (for MERS-CoV) in the same medium in a 96-well plate. Plates were incubated at 37°C for 5 days  
537 and then examined for cytopathic effect. The TCID<sub>50</sub> was calculated according to the method of

538 Spearman & Kärber. All work with infectious SARS-CoV, SARS-CoV-2 and MERS-CoV was performed in  
539 a Class II Biosafety Cabinet under BSL-3 conditions at Erasmus Medical Center.

#### 540 **SARS-CoV, SARS-CoV-2 and MERS-CoV infection**

541 Infections were performed using a protocol similar to<sup>17</sup>. Briefly, organoids were harvested in cold  
542 Advanced DMEM (including HEPES, Glutamax and antibiotics, termed AdDF+++<sup>17</sup>), washed once in  
543 AdDF+++ and sheared using a flamed Pasteur pipette in AdDF+++. Differentiated organoids were  
544 broken using a 5-minute incubation with TrypLE (TrypLE Express; Life Technologies). After shearing,  
545 organoids were washed once in AdDF+++ before infection was performed in expansion medium. For  
546 the experiment in Figure S5B, organoids were gently harvested using a wide pipet tip to avoid shearing  
547 organoids. A multiplicity of infection (MOI) of 0.1 was used for SARS-CoV and SARS-CoV-2 and an MOI  
548 of 0.2 was used for MERS-CoV. After 2 hours of virus adsorption at 37°C 5% CO<sub>2</sub>, cultures were washed  
549 four times with 4 ml AdDF+++ to remove unbound virus. Organoids were re-embedded into 30 µL BME  
550 in 48-well tissue culture plates and cultured in 250 µL expansion or differentiation medium at 37°C  
551 with 5% CO<sub>2</sub>. Each well contained ~200,000 cells per well. At indicated time points cells were harvested  
552 by resuspending the BME droplet containing organoids into 200 µL AdDF+++. Samples were stored at  
553 -80°C, a process which lysed the organoids, releasing their contents into the medium upon thawing.

554 For testing the antiviral activity of chloroquine diphosphate (Sigma), camostat mesylate (Sigma) and  
555 E64D (Medchemexpress) in intestinal organoids, sheared organoids were preincubated with these  
556 compounds in AdDF+++ at the indicated concentrations for 30 min at 37°C 5% CO<sub>2</sub> before infection at  
557 an MOI of 0.1 with SARS-CoV-2. After virus adsorption for 2 hours at 37°C 5% CO<sub>2</sub>, organoids were  
558 washed and re-embedded in BME as indicated above. Medium containing the inhibitors was added to  
559 the wells for the duration of the experiment. Cells were harvested at indicated time points as described  
560 above and stored at -80°C.

#### 561 **SARS-CoV-2 entry inhibition assay by chloroquine in VeroE6 cells**

562 Chloroquine was two-fold serially diluted in Opti-MEM I (1X) + GlutaMAX starting from a concentration  
563 of 100 µg/mL. 100 µL of each dilution was added to a confluent 96-well plate of VeroE6 cells and pre-  
564 incubated at 37°C 5% CO<sub>2</sub> for 30 minutes. Next, cells were incubated with 400 plaque-forming units of  
565 virus in the same concentration range of chloroquine at 37°C 5% CO<sub>2</sub>. After 8 hours incubation, cells  
566 were fixed with formalin, permeabilized with 70% ethanol and stained with polyclonal rabbit anti-  
567 SARS-CoV nucleoprotein antibody (1:1000; 40588-T62, Sino Biological) followed by secondary  
568 Alexa488 conjugated goat-anti-rabbit antibody (Invitrogen). Plates were scanned on the Amersham™

569 Typhoon™ Biomolecular Imager (channel Cy2; resolution 10µm; GE Healthcare). Data was analyzed  
570 using ImageQuant TL 8.2 image analysis software (GE Healthcare).

#### 571 **Determination of virus titer using qRT-PCR**

572 For determining the viral titer using qPCR, samples were thawed and centrifuged at 2,000 g for 5 min.  
573 Sixty µL supernatant was lysed in 90 µL MagnaPure LC Lysis buffer (Roche) at RT for 10 min. RNA was  
574 extracted by incubating samples with 50 µL Agencourt AMPure XP beads (Beckman Coulter) for 15 min  
575 at RT, washing beads twice with 70% ethanol on a DynaMag-96 magnet (Invitrogen) and eluting in 30  
576 µL MagnaPure LC elution buffer (Roche). Viral titers (TCID50 equivalents per mL) were determined by  
577 qRT-PCR using primer-probe sets described previously<sup>60-62</sup> and comparing the Ct values to a standard  
578 curve derived from a titrated virus stock.

#### 579 **Immunostainings and western blot**

580 Organoids were stained as described before<sup>55</sup>. Whole organoids were collected by gently dissolving  
581 the BME in ice-cold PBS, and subsequently fixed overnight at 4°C in 4% paraformaldehyde (Sigma).  
582 Next, organoids were permeabilized and blocked in PBS containing 0,5% Triton X-100 (Sigma) and 2%  
583 normal donkey serum (Jackson ImmunoResearch) for 30 min at room temperature. All stainings were  
584 performed in blocking buffer (2% normal donkey serum in PBS). For immunofluorescence, primary  
585 antibodies used were mouse anti-nucleoprotein (1:200; 40143-MM05, Sino Biological), mouse anti-  
586 dsRNA (1:200; Scicons), goat anti-ACE (1:100; R&D Systems, AF933), goat anti-DPP-4 (1:200; R&D  
587 systems, AF1180) and rabbit anti-MERS S1 (1:200; 40069-T52, Sino Biological). For  
588 immunofluorescence, organoids were incubated with the corresponding secondary antibodies  
589 Alexa488-, 568- and 647-conjugated anti-rabbit and anti-goat (1:1,000; Molecular Probes) or  
590 Phalloidin-Alexa488 (Thermofisher Scientific) in blocking buffer containing 4',6-diamidino-2-  
591 phenylindole (DAPI; 1;1,000, Invitrogen). After staining, organoids were transfected to a glass slide  
592 embedded in Vectashield (Vector labs). Stained organoids were imaged using a SP8 confocal  
593 microscope (Leica) or a Zeiss LSM700, and image analysis and presentation was performed using  
594 ImageJ software.

595 Immunohistochemistry was performed as described before<sup>63</sup>. Antigen retrieval for TMPRSS2 staining  
596 was achieved by boiling for 20 minutes in citrate buffer. Primary antibody used was rabbit anti-  
597 TMPRSS2 (1:100; Abcam, ab109131) followed by anti-rabbit conjugated to horseradish peroxidase  
598 (Povervision, Leica)

599 For Western blot of CTSL, organoid proteins were solubilized using a standard RIPA buffer for 30 min  
600 on ice in the presence of protease inhibitors. Samples were run on a 4-15% PAA gel (BioRad) under  
601 reducing conditions. Proteins were electrophoresed to PVDF membranes from Immobilon. Both  
602 primary antibodies, mouse anti-CTSL ( $\pm$  25 kDa) and mouse anti-ITGB4 ( $\pm$  200 kDa), were incubated  
603 O/N at 4C in PBS/10% milk protein/0.1% Tween20. The secondary rabbit anti-mouse HRP-conjugate  
604 (Dako) was incubated for 2hrs at 4C in the same buffer. The mouse IgG2a antibody against ITGB4,  
605 58XB4, was a gift from A. Sonnenberg (NKI, Amsterdam, The Netherlands). HRP activity was visualized  
606 with ECL (GE-Healthcare).

607

### 608 **Bulk RNA sequencing**

609 Single Cell Discoveries (Utrecht, The Netherlands) performed library preparation, using an adapted  
610 version of the CEL-seq protocol, as we have done previously<sup>17</sup>. After library generation, paired-end  
611 sequencing was performed on the Illumina Nextseq500 platform using barcoded 1 x 75 nt read setup.  
612 Read 1 was used to identify the Illumina library index and CEL-Seq sample barcode. Read 2 was aligned  
613 to the CRCh38 human RefSeq transcriptome, with the addition SARS-CoV-2 (Ref-SKU: 026V-03883) or  
614 MERS (NC\_038294.1) genomes, using BWA using standard settings<sup>64</sup>. Reads that mapped equally well  
615 to multiple locations were discarded. Mapping and generation of count tables was performed using  
616 the in-house MapAndGo script, filtering to exclude reads with identical library- and molecule-barcodes.  
617 RNA sequencing data from expanding and differentiated human intestinal organoids, infected with  
618 SARS-CoV-2, was used from a previous publication<sup>17</sup>. Normalization using the median of ratios method  
619 and differential gene expression analysis was performed using the DESeq2 package<sup>64</sup>. SARS- and MERS-  
620 mapping reads were removed before normalization to avoid biasing organoid transcript counts. To  
621 generate heatmaps, row z-scores of selected genes were calculated from the samples selected.

622

### 623 **Organoid preparation for single cell sequencing analysis**

624 Human ileal organoids were differentiated as previously described<sup>56</sup>. A control condition was kept  
625 in human organoid expansion medium to obtain stem- and progenitor cells for comparison.

626 Dissociation of organoids to single cells was performed by a 10-minute incubation with TrypLE (TrypLE  
627 Express; Life Technologies) supported by repeated mechanical disruption using a narrowed glass  
628 pipette. Viable cells were sorted using a BD FACS Aria (BD Biosciences) using DAPI exclusion. Individual  
629 cells were collected in 384-well plates with ERCC spike-ins (Agilent), reverse transcription primers and  
630 dNTPs (both Promega). Single cell sequencing was performed according to the Sort-seq method<sup>65</sup>.

631 Sequencing libraries were generated with TruSeq small RNA primers (Illumina) and sequenced paired-  
632 end at 60 and 26 bp read length, respectively, on the Illumina NextSeq.

### 633 **Single cell RNA sequencing analysis from intestinal organoids and tissue**

634 Reads derived from 1344 cells (192 expansion medium, 1152 differentiation medium) were mapped  
635 to the human GRCh37 genome assembly. Sort-seq read counts were filtered to exclude reads with  
636 identical library-, cell- and molecule barcodes. UMI counts were adjusted using Poisson counting  
637 statistics<sup>65</sup>. Cells with fewer than 1,000 unique transcripts were excluded from further analysis. This  
638 resulted in 944 remaining cells (126 from expansion, 818 from differentiation medium)

639 Subsequently, RaceID3 was used for k-medoids-based clustering (knn = 5; cln = 20) of cells and  
640 differential gene expression analysis between clusters using the standard settings described at  
641 [https://github.com/dgrun/RaceID3\\_StemID2\\_package](https://github.com/dgrun/RaceID3_StemID2_package). Cell types were annotated by cluster based on  
642 the expression of marker genes (OLFM4 for stem cells, FABP1 for enterocytes, FCGBP for goblet cells.  
643 Lack of these and expression of cell cycle markers including PCNA defined proliferating progenitors  
644 cells).

645 For comparison with tissue-derived cells, we reanalyzed a previously published dataset<sup>32</sup> of primary  
646 human ileal cell types. To compare with the organoid data set, cells were required to be annotated as  
647 stem cell, progenitor cell, goblet cell or enterocyte and exhibit more than 3,000 unique transcripts.  
648 This resulted in 2137 included cells, which were subsequently clustered using the standard settings of  
649 RaceID3 (cln = 16). Cells were assigned an identity based on their annotation from<sup>32</sup>.

### 650 **Quantification and statistics**

651 No statistical methods were used to predetermine sample size. The experiments were not randomized  
652 and the investigators were not blinded to the sample allocation during experiments and outcome  
653 assessment. All data are presented as mean  $\pm$  standard error of the mean (SEM), unless stated  
654 otherwise. Value of n is always displayed in the figure as individual data points, and in the legends.

655 Statistical analysis was performed with the GraphPad Prism 9 software. We compared differences in  
656 virus replication and organoid growth by one-way ANOVA followed by a multiple-comparison test  
657 (Original FDR method of Benjamini and Hochberg; Q = 0.05) on log<sub>10</sub> transformed values. Statistics  
658 were applied if N  $\geq$  3.

### 659 **Data availability statement**

660 All bulk and single cell RNA sequencing data of this study has been uploaded to the Gene Expression  
661 Omnibus (GEO), and will be publically available upon publication (GEO accession number is pending).

## 662 **References**

- 663 1. Zhou, P. *et al.* A pneumonia outbreak associated with a new coronavirus of probable bat  
664 origin. *Nature* **579**, 270–273 (2020).
- 665 2. Hulswit, R. J. G., de Haan, C. A. M. & Bosch, B. J. Coronavirus Spike Protein and Tropism  
666 Changes. in *Advances in Virus Research* **96**, 29–57 (2016).
- 667 3. Kaye, M. *et al.* SARS-associated Coronavirus Replication in Cell Lines. *Emerg. Infect. Dis.*  
668 (2006). doi:10.3201/eid1201.050496
- 669 4. Hoffmann, M. *et al.* SARS-CoV-2 Cell Entry Depends on ACE2 and TMPRSS2 and Is Blocked by a  
670 Clinically Proven Protease Inhibitor. *Cell* **181**, 271-280.e8 (2020).
- 671 5. Li, W. *et al.* Angiotensin-converting enzyme 2 is a functional receptor for the SARS  
672 coronavirus. *Nature* (2003). doi:10.1038/nature02145
- 673 6. Raj, V. S. *et al.* Dipeptidyl peptidase 4 is a functional receptor for the emerging human  
674 coronavirus-EMC. *Nature* (2013). doi:10.1038/nature12005
- 675 7. Wang, M. *et al.* Remdesivir and chloroquine effectively inhibit the recently emerged novel  
676 coronavirus (2019-nCoV) in vitro. *Cell Research* (2020). doi:10.1038/s41422-020-0282-0
- 677 8. Boulware, D. R. *et al.* A Randomized Trial of Hydroxychloroquine as Postexposure Prophylaxis  
678 for Covid-19. *N. Engl. J. Med.* (2020). doi:10.1056/NEJMoa2016638
- 679 9. Wei, J. *et al.* Genome-wide CRISPR Screens Reveal Host Factors Critical for SARS-CoV-2  
680 Infection. *Cell* (2020). doi:10.1016/j.cell.2020.10.028
- 681 10. Zhu, Y. *et al.* A genome-wide CRISPR screen identifies host factors that regulate SARS-CoV-2  
682 entry. *Nat. Commun.* (2021). doi:10.1038/s41467-021-21213-4
- 683 11. Mykytyn, A. Z. *et al.* The SARS-CoV-2 multibasic cleavage site facilitates early serine protease-  
684 mediated entry into organoid-derived human airway cells 2 3. *bioRxiv* (2020).
- 685 12. Clausen, T. M. *et al.* SARS-CoV-2 Infection Depends on Cellular Heparan Sulfate and ACE2. *Cell*  
686 (2020). doi:10.1016/j.cell.2020.09.033
- 687 13. Cantuti-Castelvetri, L. *et al.* Neuropilin-1 facilitates SARS-CoV-2 cell entry and infectivity.  
688 *Science* (80-. ). **370**, (2020).

- 689 14. Daly, J. L. *et al.* Neuropilin-1 is a host factor for SARS-CoV-2 infection. *Science* **370**, 861–865  
690 (2020).
- 691 15. Shang, J. *et al.* Cell entry mechanisms of SARS-CoV-2. *Proc. Natl. Acad. Sci. U. S. A.* (2020).  
692 doi:10.1073/pnas.2003138117
- 693 16. Yang, L. *et al.* A Human Pluripotent Stem Cell-based Platform to Study SARS-CoV-2 Tropism  
694 and Model Virus Infection in Human Cells and Organoids. *Cell Stem Cell* (2020).  
695 doi:10.1016/j.stem.2020.06.015
- 696 17. Lamers, M. M. *et al.* SARS-CoV-2 productively infects human gut enterocytes. *Science* (2020).  
697 doi:10.1126/science.abc1669
- 698 18. Zhou, J. *et al.* Infection of bat and human intestinal organoids by SARS-CoV-2. *Nat. Med.*  
699 (2020). doi:10.1038/s41591-020-0912-6
- 700 19. Cholankeril, G. *et al.* High Prevalence of Concurrent Gastrointestinal Manifestations in  
701 Patients With Severe Acute Respiratory Syndrome Coronavirus 2: Early Experience From  
702 California. *Gastroenterology* (2020). doi:10.1053/j.gastro.2020.04.008
- 703 20. Gu, J., Han, B. & Wang, J. COVID-19: Gastrointestinal Manifestations and Potential Fecal–Oral  
704 Transmission. *Gastroenterology* (2020). doi:10.1053/j.gastro.2020.02.054
- 705 21. Drost, J. *et al.* Sequential cancer mutations in cultured human intestinal stem cells. *Nature*  
706 **521**, 43–47 (2015).
- 707 22. Millet, J. K. & Whittaker, G. R. Host cell proteases: Critical determinants of coronavirus  
708 tropism and pathogenesis. *Virus Res.* (2015). doi:10.1016/j.virusres.2014.11.021
- 709 23. Simmons, G., Zmora, P., Gierer, S., Heurich, A. & Pöhlmann, S. Proteolytic activation of the  
710 SARS-coronavirus spike protein: Cutting enzymes at the cutting edge of antiviral research.  
711 *Antiviral Research* **100**, 605–614 (2013).
- 712 24. Nomura, R. *et al.* Human Coronavirus 229E Binds to CD13 in Rafts and Enters the Cell through  
713 Caveolae. *J. Virol.* **78**, 8701–8708 (2004).
- 714 25. Sung, P. S. & Hsieh, S. L. CLEC2 and CLEC5A: Pathogenic Host Factors in Acute Viral Infections.  
715 *Frontiers in Immunology* **10**, (2019).
- 716 26. Yu, Y. T. C. *et al.* Surface vimentin is critical for the cell entry of SARS-CoV. *J. Biomed. Sci.* **23**,  
717 (2016).



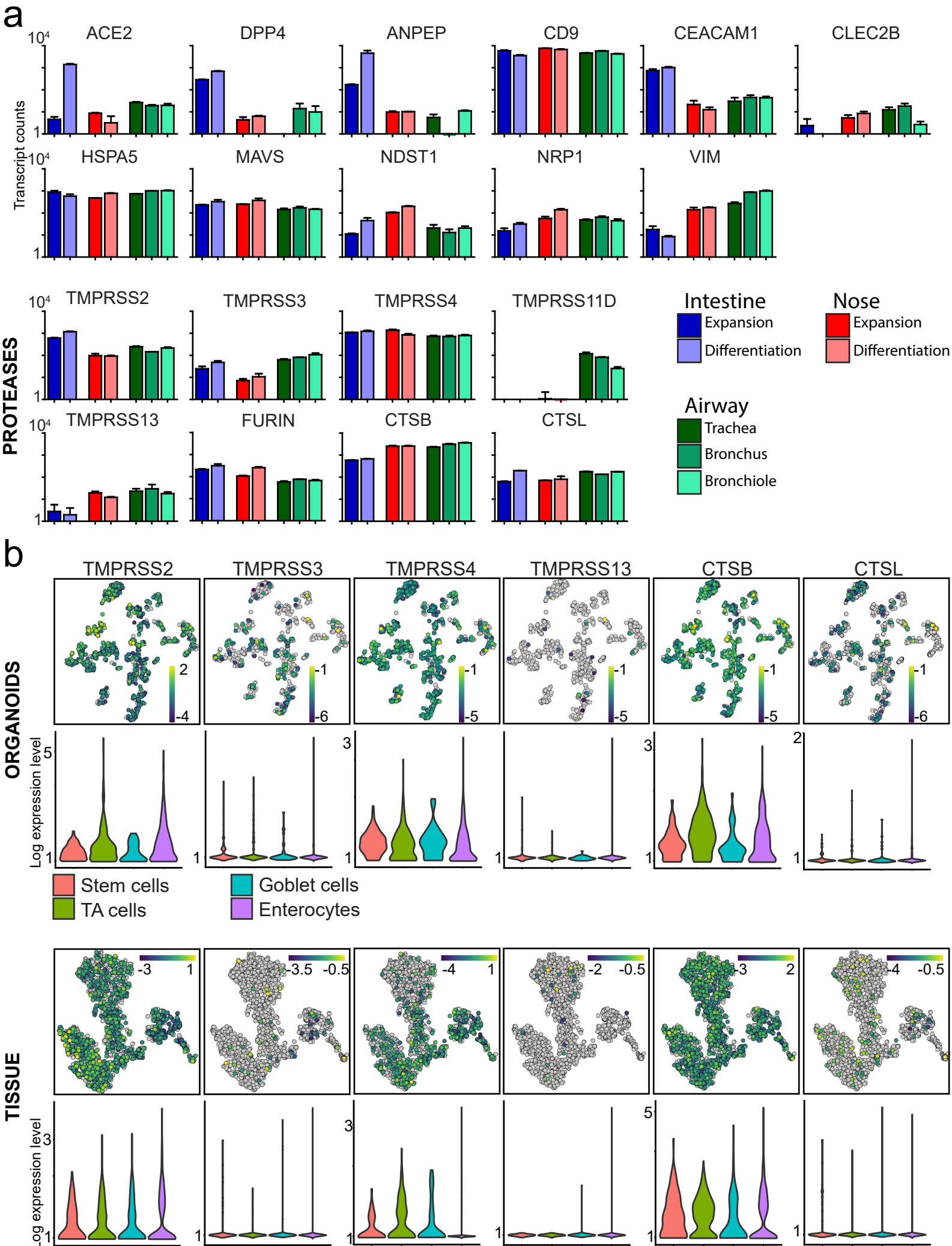
- 718 27. Miura, H. S., Nakagaki, K. & Taguchi, F. N-Terminal Domain of the Murine Coronavirus  
719 Receptor CEACAM1 Is Responsible for Fusogenic Activation and Conformational Changes of  
720 the Spike Protein. *J. Virol.* (2004). doi:10.1128/jvi.78.1.216-223.2004
- 721 28. Earnest, J. T. *et al.* The tetraspanin CD9 facilitates MERS-coronavirus entry by scaffolding host  
722 cell receptors and proteases. *PLoS Pathog.* **13**, (2017).
- 723 29. Marzi, A. *et al.* DC-SIGN and DC-SIGNR Interact with the Glycoprotein of Marburg Virus and  
724 the S Protein of Severe Acute Respiratory Syndrome Coronavirus. *J. Virol.* **78**, 12090–12095  
725 (2004).
- 726 30. Shi, C.-S. *et al.* SARS-Coronavirus Open Reading Frame-9b Suppresses Innate Immunity by  
727 Targeting Mitochondria and the MAVS/TRAF3/TRAF6 Signalosome. *J. Immunol.* **193**, 3080–  
728 3089 (2014).
- 729 31. Chu, H. *et al.* Middle East respiratory syndrome coronavirus and bat coronavirus HKU9 both  
730 can utilize GRP78 for attachment onto host cells. *J. Biol. Chem.* (2018).  
731 doi:10.1074/jbc.RA118.001897
- 732 32. Wang, Y. *et al.* Single-cell transcriptome analysis reveals differential nutrient absorption  
733 functions in human intestine. *J. Exp. Med.* (2020). doi:10.1084/jem.20191130
- 734 33. Zang, R. *et al.* TMPRSS2 and TMPRSS4 promote SARS-CoV-2 infection of human small  
735 intestinal enterocytes. *Sci. Immunol.* (2020). doi:10.1126/sciimmunol.abc3582
- 736 34. Wang, T. *et al.* Identification and characterization of essential genes in the human genome.  
737 *Science (80-. ).* **350**, 1096–1101 (2015).
- 738 35. Winkler, E. S. *et al.* SARS-CoV-2 infection of human ACE2-transgenic mice causes severe lung  
739 inflammation and impaired function. *Nat. Immunol.* (2020). doi:10.1038/s41590-020-0778-2
- 740 36. Amraie, R. *et al.* CD209L/L-SIGN and CD209/DC-SIGN act as receptors for SARS-CoV-2 and are  
741 differentially expressed in lung and kidney epithelial and endothelial cells. *bioRxiv Prepr. Serv.*  
742 *Biol.* (2020). doi:10.1101/2020.06.22.165803
- 743 37. Triana, S. *et al.* Single-cell analyses reveal SARS-CoV-2 interference with intrinsic immune  
744 response in the human gut. *Mol. Syst. Biol.* **17**, e10232 (2021).
- 745 38. Kindler, E., Thiel, V. & Weber, F. Interaction of SARS and MERS Coronaviruses with the  
746 Antiviral Interferon Response. in *Advances in Virus Research* (2016).  
747 doi:10.1016/bs.aivir.2016.08.006

- 748 39. Lamers, M. M. *et al.* Human airway cells prevent SARS-CoV-2 multibasic cleavage site cell  
749 culture adaptation. *Elife* (2021). doi:10.7554/elife.66815
- 750 40. Klimstra, W. B. *et al.* SARS-CoV-2 growth, furin-cleavage-site adaptation and neutralization  
751 using serum from acutely infected hospitalized COVID-19 patients. *J. Gen. Virol.* (2020).  
752 doi:10.1099/jgv.0.001481
- 753 41. Ogando, N. S. *et al.* SARS-coronavirus-2 replication in Vero E6 cells: Replication kinetics, rapid  
754 adaptation and cytopathology. *J. Gen. Virol.* (2020). doi:10.1099/jgv.0.001453
- 755 42. Davidson, A. D. *et al.* Characterisation of the transcriptome and proteome of SARS-CoV-2  
756 reveals a cell passage induced in-frame deletion of the furin-like cleavage site from the spike  
757 glycoprotein. *Genome Med.* (2020). doi:10.1186/s13073-020-00763-0
- 758 43. Peacock, T. P. *et al.* The furin cleavage site in the SARS-CoV-2 spike protein is required for  
759 transmission in ferrets. *Nat. Microbiol.* (2021). doi:10.1038/s41564-021-00908-w
- 760 44. Graham, M. S. *et al.* Changes in symptomatology, reinfection, and transmissibility associated  
761 with the SARS-CoV-2 variant B.1.1.7: an ecological study. *Lancet Public Heal.* (2021).  
762 doi:10.1016/s2468-2667(21)00055-4
- 763 45. Frampton, D. *et al.* Genomic characteristics and clinical effect of the emergent SARS-CoV-2  
764 B.1.1.7 lineage in London, UK: a whole-genome sequencing and hospital-based cohort study.  
765 *Lancet Infect. Dis.* (2021). doi:10.1016/s1473-3099(21)00170-5
- 766 46. Volz, E. *et al.* Assessing transmissibility of SARS-CoV-2 lineage B.1.1.7 in England. *Nature*  
767 (2021). doi:10.1038/s41586-021-03470-x
- 768 47. WHO Solidarity Trial Consortium *et al.* Repurposed Antiviral Drugs for Covid-19 - Interim WHO  
769 Solidarity Trial Results. *N. Engl. J. Med.* (2020). doi:10.1056/NEJMoa2023184
- 770 48. Vincent, M. J. *et al.* Chloroquine is a potent inhibitor of SARS coronavirus infection and  
771 spread. *Viol. J.* **2**, (2005).
- 772 49. Daniloski, Z. *et al.* Identification of Required Host Factors for SARS-CoV-2 Infection in Human  
773 Cells. *Cell* (2020). doi:10.1016/j.cell.2020.10.030
- 774 50. Schneider, W. M. *et al.* Genome-scale identification of SARS-CoV-2 and pan-coronavirus host  
775 factor networks. *Cell* (2020). doi:10.1016/j.cell.2020.12.006
- 776 51. Hoffmann, M. *et al.* Camostat mesylate inhibits SARS-CoV-2 activation by TMPRSS2-related  
777 proteases and its metabolite GBPA exerts antiviral activity. *EBioMedicine* (2021).

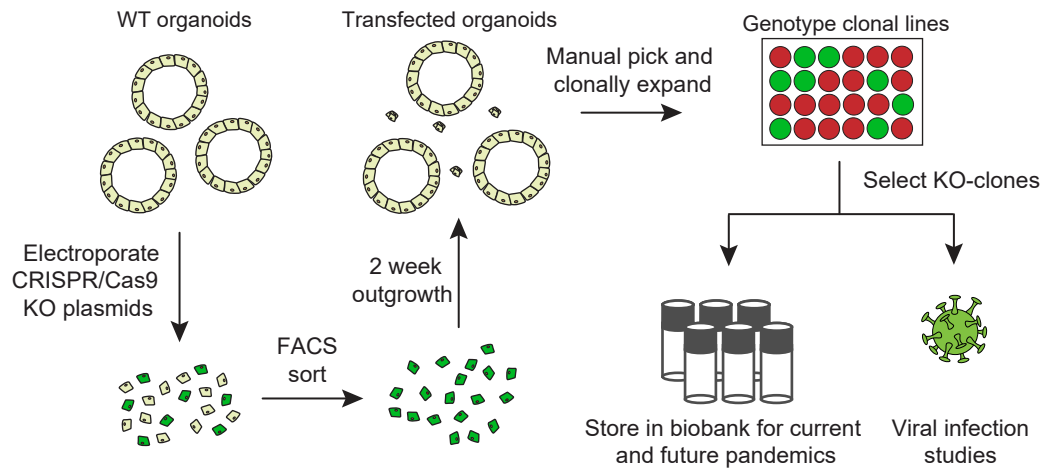
- 778 doi:10.1016/j.ebiom.2021.103255
- 779 52. Singh, M., Bansal, V. & Feschotte, C. A Single-Cell RNA Expression Map of Human Coronavirus  
780 Entry Factors. *Cell Rep.* (2020). doi:10.1016/j.celrep.2020.108175
- 781 53. Kim, T. S., Heinlein, C., Hackman, R. C. & Nelson, P. S. Phenotypic Analysis of Mice Lacking the  
782 Tmprss2-Encoded Protease. *Mol. Cell. Biol.* **26**, 965–975 (2006).
- 783 54. Iwata-Yoshikawa, N. *et al.* TMPRSS2 Contributes to Virus Spread and Immunopathology in the  
784 Airways of Murine Models after Coronavirus Infection. *J. Virol.* **93**, (2019).
- 785 55. Beumer, J. *et al.* Enteroendocrine cells switch hormone expression along the crypt-to-villus  
786 BMP signalling gradient. *Nature Cell Biology* **20**, 909–916 (2018).
- 787 56. Sato, T. *et al.* Long-term expansion of epithelial organoids from human colon, adenoma,  
788 adenocarcinoma, and Barrett’s epithelium. *Gastroenterology* **141**, 1762–1772 (2011).
- 789 57. Sachs, N. *et al.* Long-term expanding human airway organoids for disease modeling. *EMBO J.*  
790 **38**, (2019).
- 791 58. Ran, F. A. *et al.* Genome engineering using the CRISPR-Cas9 system. *Nat Protoc.* **8**, (2013).
- 792 59. Fujii, M., Matano, M., Nanki, K. & Sato, T. Efficient genetic engineering of human intestinal  
793 organoids using electroporation. *Nat. Protoc.* **10**, 1474–1485 (2015).
- 794 60. Corman, V. M. *et al.* Detection of a novel human coronavirus by real-time reverse-  
795 transcription polymerase chain reaction. *Eurosurveillance* (2012).  
796 doi:10.2807/ese.17.39.20285-en
- 797 61. Corman, V. M. *et al.* Detection of 2019 novel coronavirus (2019-nCoV) by real-time RT-PCR.  
798 *Eurosurveillance* (2020). doi:10.2807/1560-7917.ES.2020.25.3.2000045
- 799 62. Kuiken, T. *et al.* Newly discovered coronavirus as the primary cause of severe acute  
800 respiratory syndrome. *Lancet* **362**, 263–270 (2003).
- 801 63. Muncan, V. *et al.* Rapid Loss of Intestinal Crypts upon Conditional Deletion of the Wnt/Tcf-4  
802 Target Gene c-Myc. *Mol. Cell. Biol.* (2006). doi:10.1128/mcb.00821-06
- 803 64. Love, M. I., Huber, W. & Anders, S. Moderated estimation of fold change and dispersion for  
804 RNA-seq data with DESeq2. *Genome Biol.* **15**, 550 (2014).
- 805 65. Muraro, M. J. *et al.* A Single-Cell Transcriptome Atlas of the Human Pancreas. *Cell Syst.* **3**, 385–  
806 394 (2016).



Figure 1 Expression levels of potential host genes and proteases in lung and intestinal organoids and tissue



a



b

	Ileum		Duodenum	
		Number of KO clones		Number of KO clones
	Wildtype	4	Wildtype	2
RECEPTORS	ACE2	4	ACE2	4
	DPP4	4		
	NRP1	4		
	ANPEP	3		
	DC-SIGN	4		
	CD9	2		
PROTEASES	TMPRSS2	4	TMPRSS2	4
	TMPRSS3	4		
	TMPRSS4	4		
	TMPRSS11D	5		
	TMPRSS13	6		
	FURIN	1		
	CTSB	6		
	CTSL	2		
OTHER	ARC	1		
	CLEC2B	2		
	MAVS	2		
	VIMENTIN	2		
	HSPA5	0		
	NDST1	2		

c

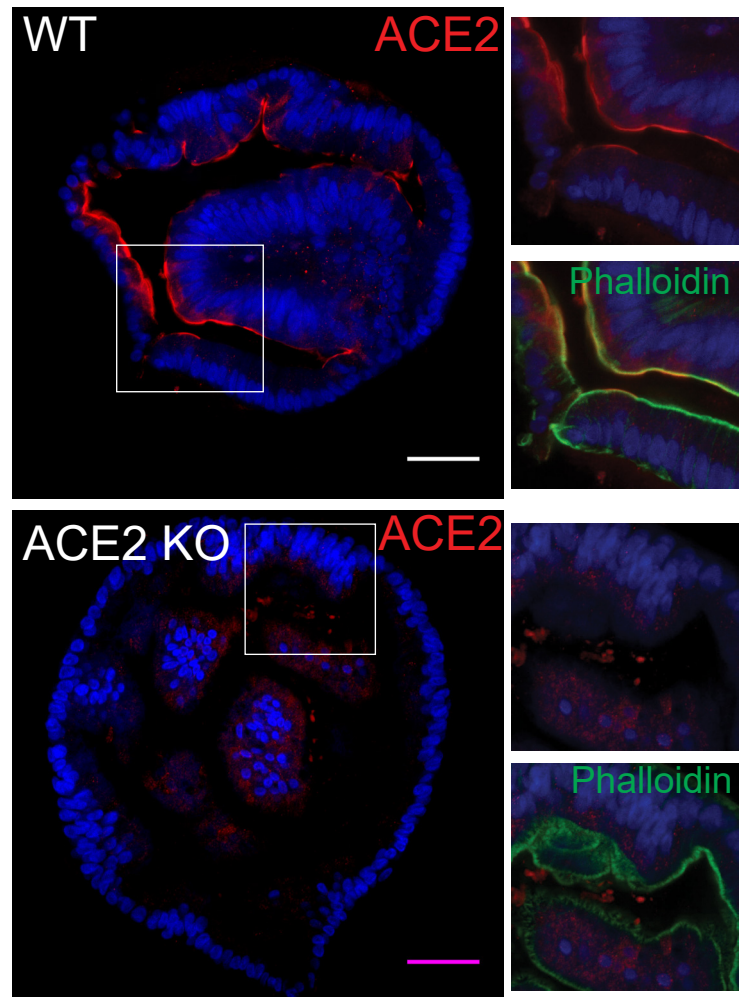
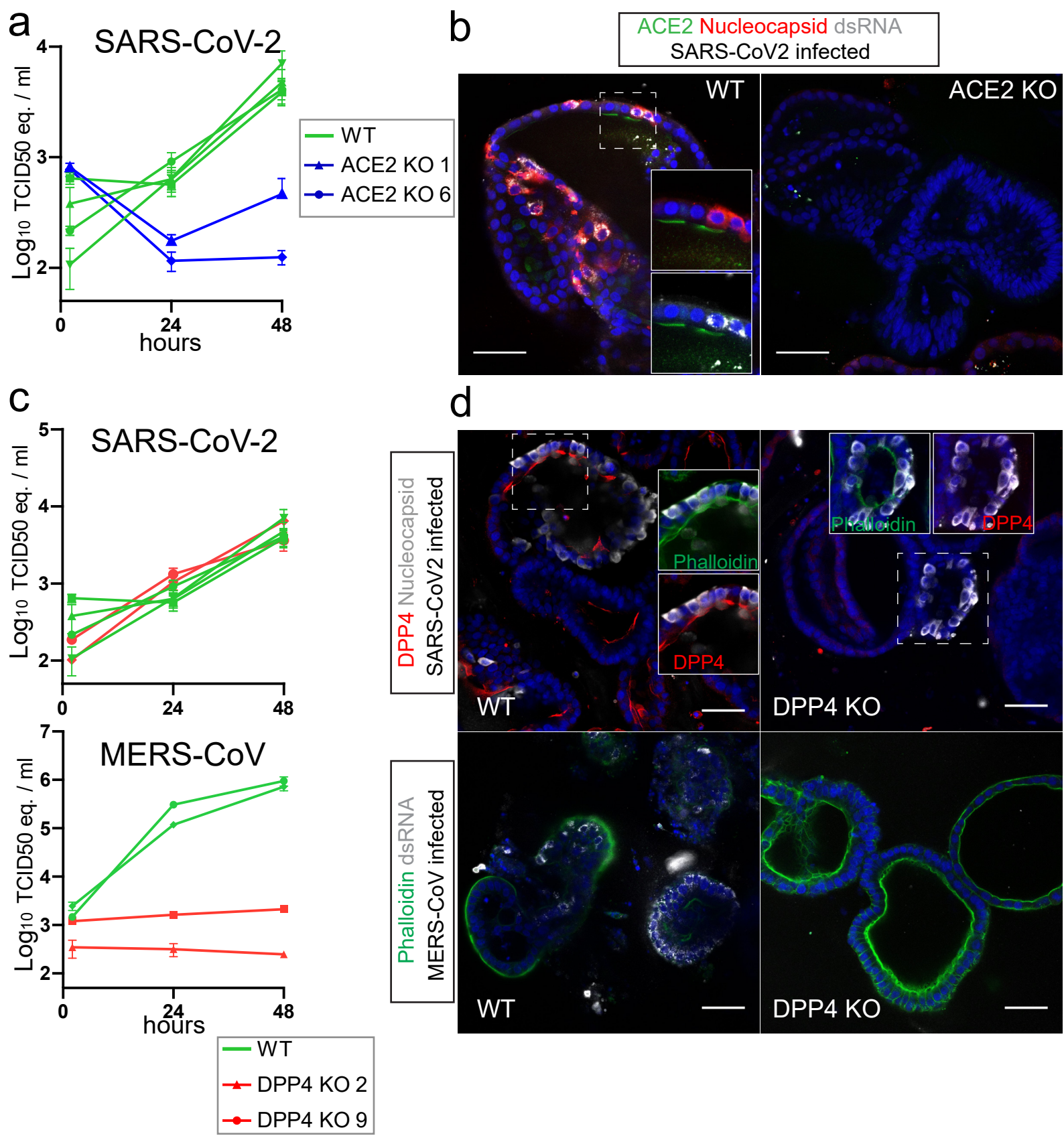
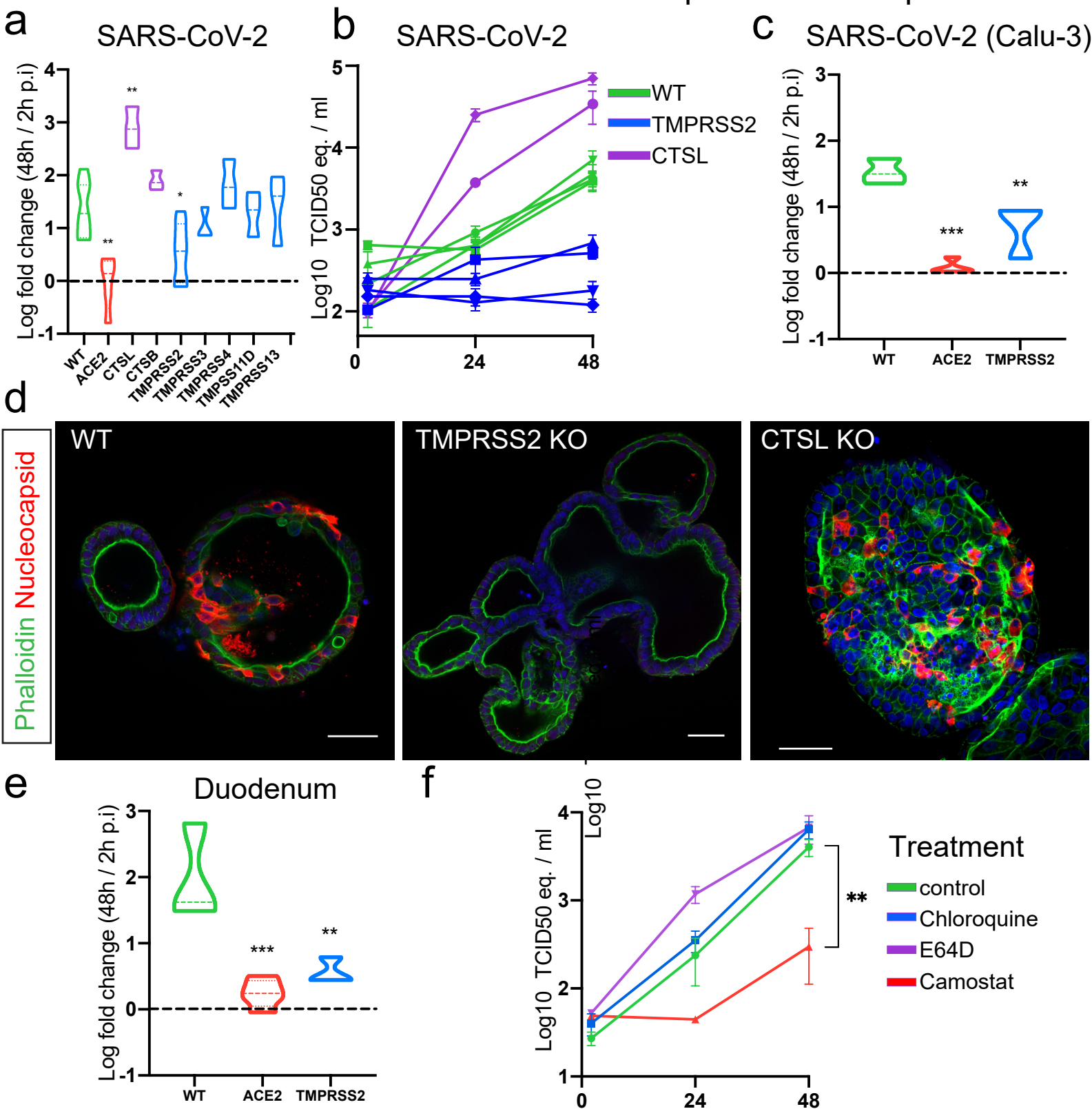


# Figure 3 ACE2 and DPP4 are the obligate entry receptors for SARS-CoV-2 and MERS-CoV respectively



bioRxiv preprint doi: <https://doi.org/10.1101/2021.05.20.445723>; this version posted May 20, 2021. The copyright holder for this preprint (which was not certified by peer review) is the author/funder. All rights reserved. No reuse allowed without permission.

# Figure 4 Loss of function screen of host proteases reveals essential role for TMPRSS2 but not Cathepsins in viral replication





bioRxiv preprint doi: <https://doi.org/10.1101/2021.05.20.449753>; this version posted May 20, 2021. The copyright holder for this preprint (which was not certified by peer review) is the author/funder. All rights reserved. No reuse allowed without permission.

# Figure 5 Replication of SARS-CoV-2 is not altered by loss of different host factors

of different host factors

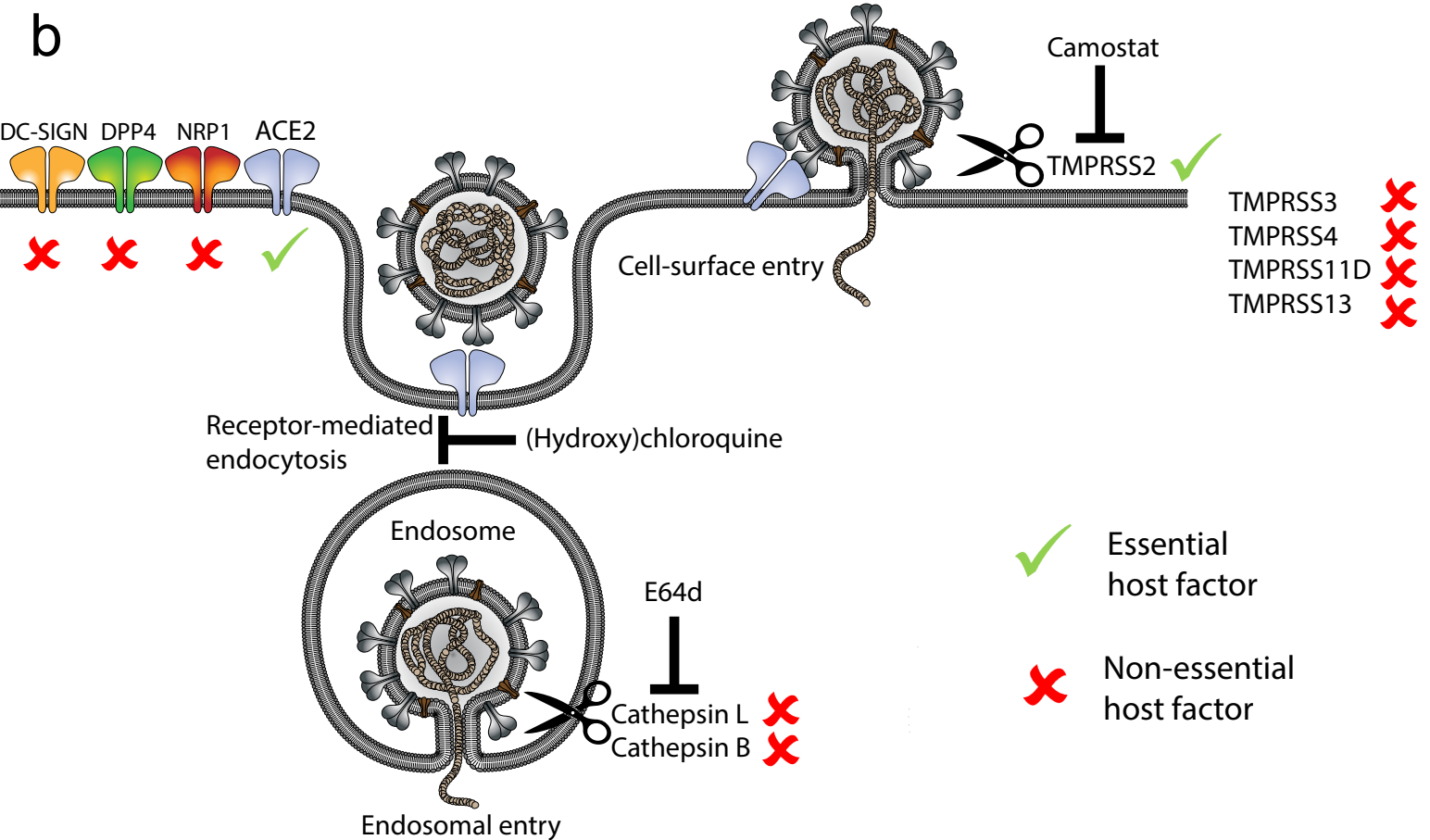
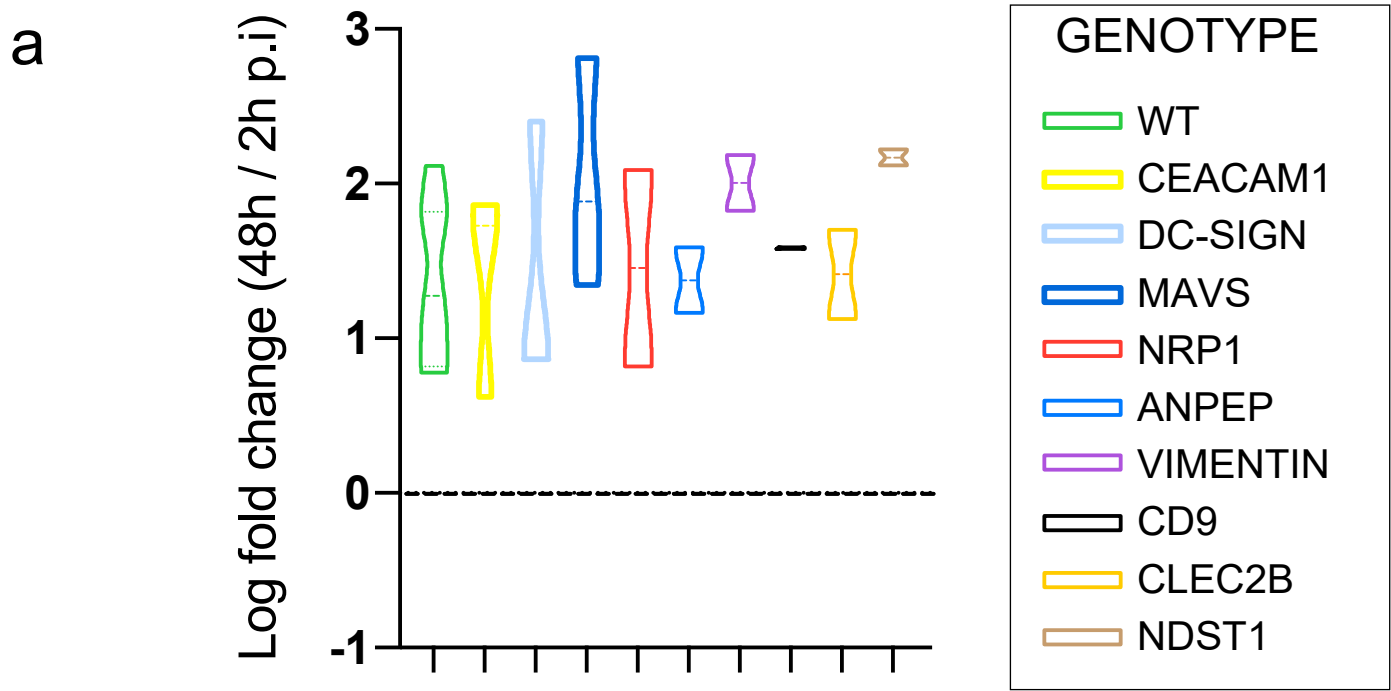
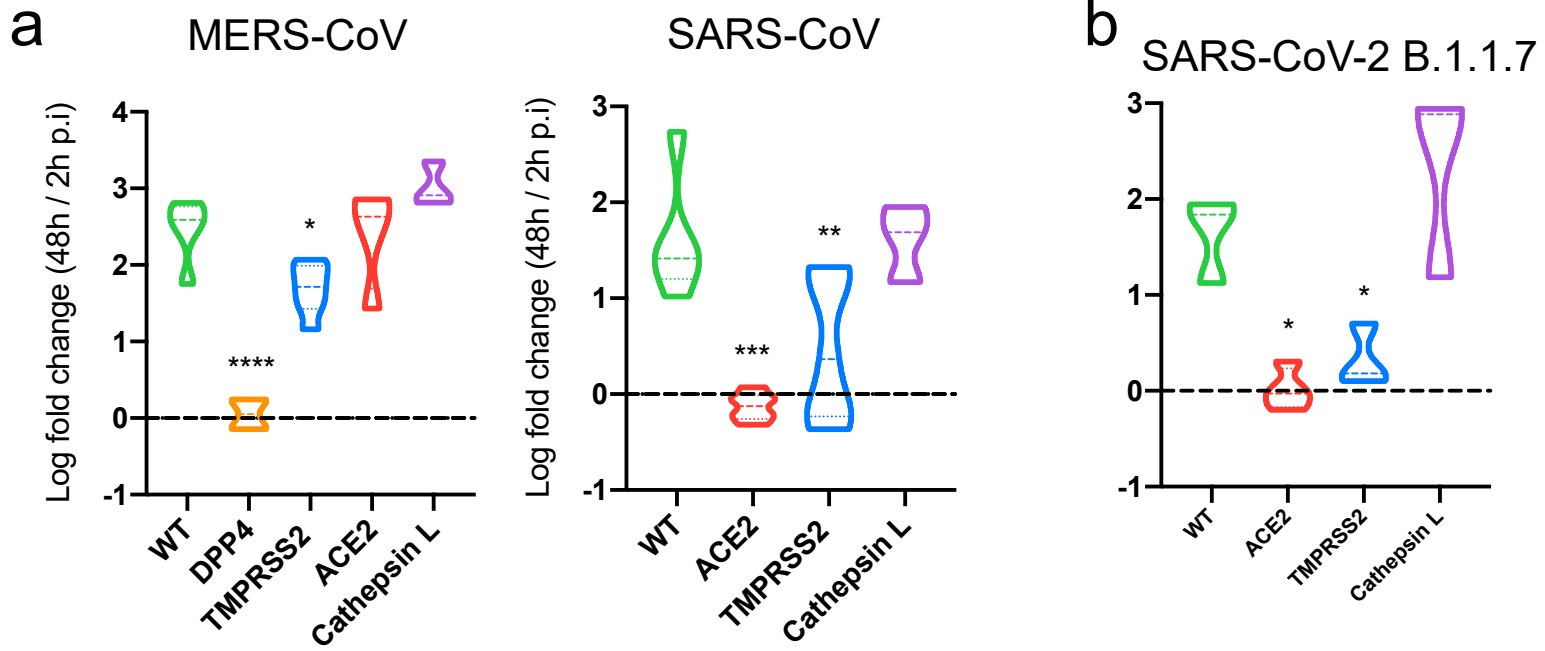
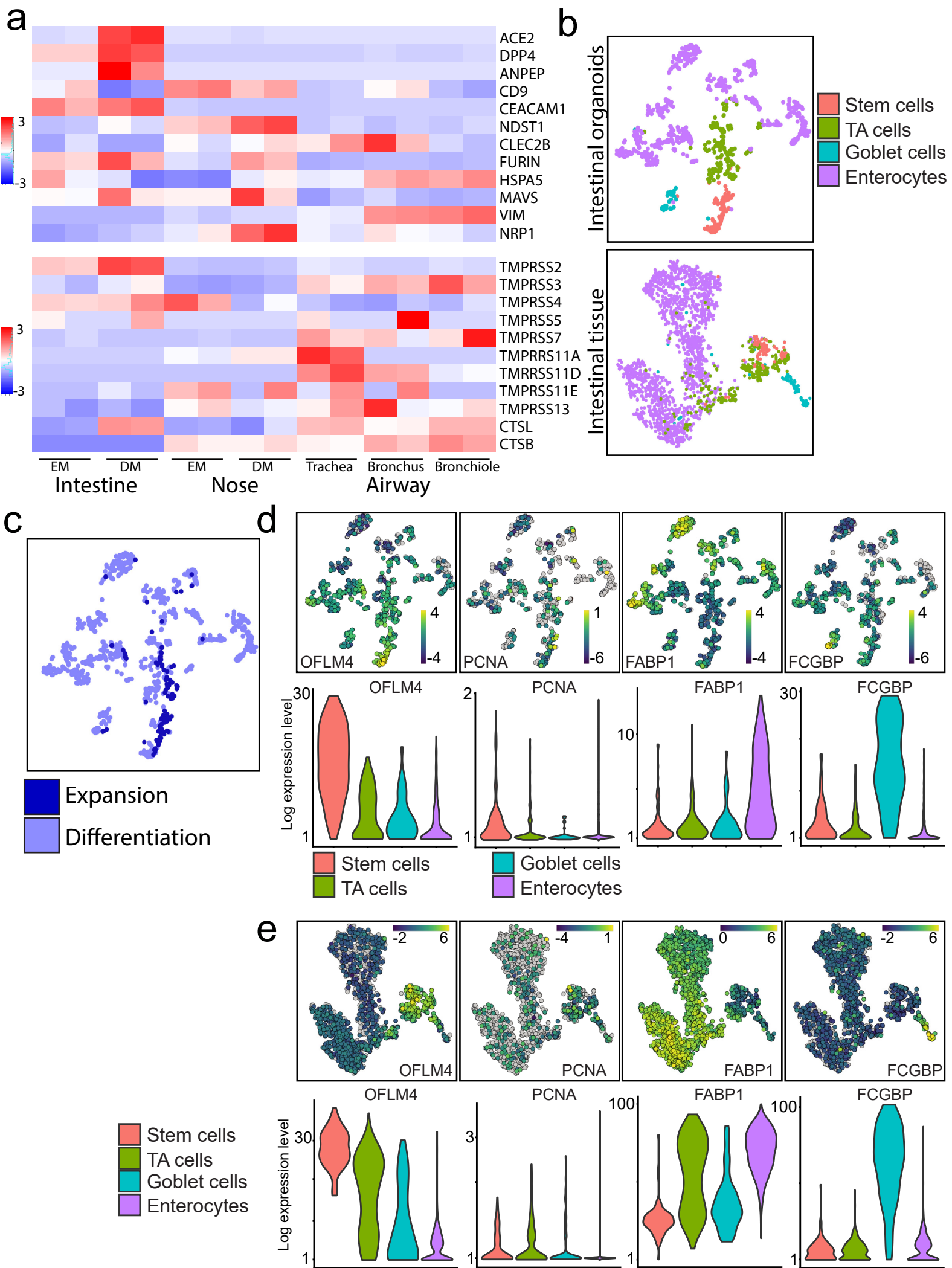


## Figure 6 Host protease dependency in the SARS-CoV-2 strain B.1.1.7 and other coronaviruses

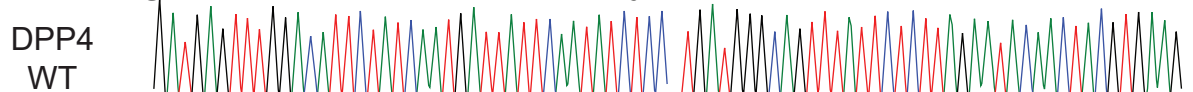


Supplementary figure 1 Bulk and single-cell RNA sequencing reveals intestinal expression of host proteases involved in viral entry

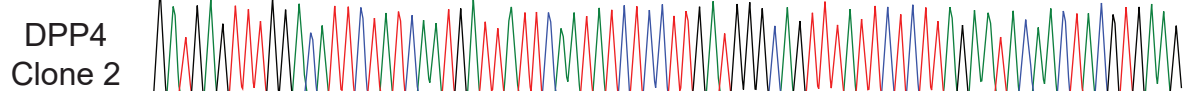




# Supplementary figure 3 Organoid genotyping by sanger sequencing and in silico ICE analysis.



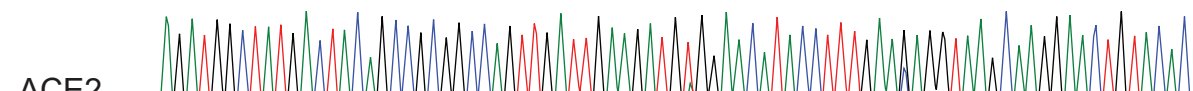
GATGAGTTTGGACATTCTATCAATGATTATTCAATATCTCC-TGATGGGCAGTTTATTCTCTTAGAATACAACACTACGTGAAG



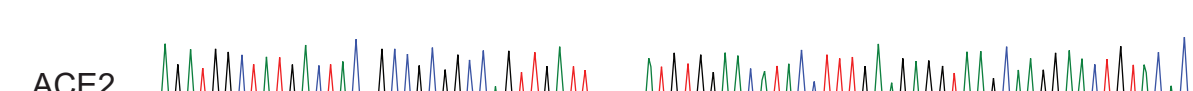
GATGAGTTTGGACATTCTATCAATGATTATTCAATATCTCCTTGATGGGCAGTTTATTCTCTTAGAATACAACACTACGTGAAG

INDEL CONTRIBUTION SEQUENCE

+1 99% TATCAATGATTATTCAATATCTCTCT; NGATGGGCAGTTTATTCTCTTAGA



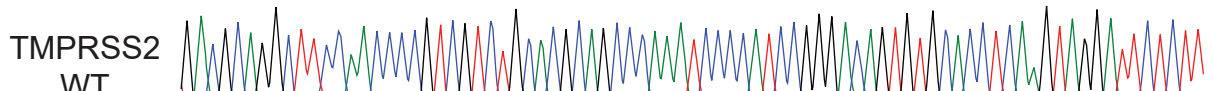
AGATGGCTATGACTACAGCCGCGGCCAGTTGATTGAAGATGTGGAACATACCTTTGAAGAGGTAAGCAAGGAAGCTGTACAC



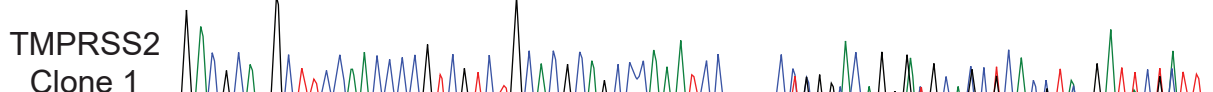
AGATGGCTATGACTACAGCCGCGGCCAGTTGATTATGTTGAACATACCTTTGAAGAGGTAAGCAAGGAAGCTGTACAC

INDEL CONTRIBUTION SEQUENCE

-4 89% TACAGCCGCGGCCAGTTGATT; ATGTTGAACATACCTTTGAAGAGGTTAA  
-4 3% TACAGCCGCGGCCAGTTGATTG; -TGTGGAACATACCTTTGAAGAGGTTAA  
-4 1% TACAGCCGCGGCCAGTTGATTGAA; -TGGAAACATACCTTTGAAGAGGTTAA



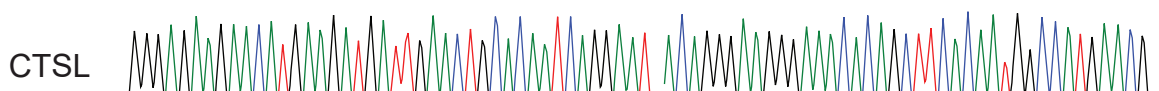
GACGCAGGCTTCCAACCCCGTCGTCTGCACGCAGCCCAAATCCCCATCCGGGACAGTGTGCACCTCAAGTAGGATTCTCTT



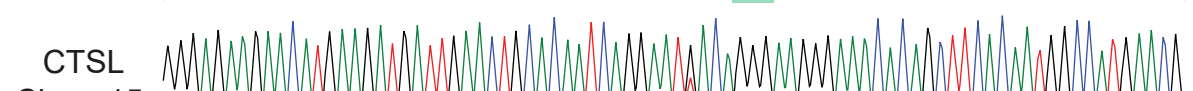
GACGCAGGCTTCCAACCCCGTCGTCTGCACGCAGCCCAAATCCCGGACAGGGCGCAGCTCACCTAAGATTCTATT

INDEL CONTRIBUTION SEQUENCE

-4 57% TCGTCTGCACGCAGCCCAAATCCCC; GGGACAGTGTGTCACCTCAAG  
+1 35% TCGTCTGCACGCAGCCCAAATCCCC; NATCCGGGACAGTGTGTCACCTCAA



GGGAGAAGAACATGAAGATGATTGAAGTGCACAATCAGGAAT-ACAGGGAAAGGAAACACAGCTTCACAATGGCCATGAACG



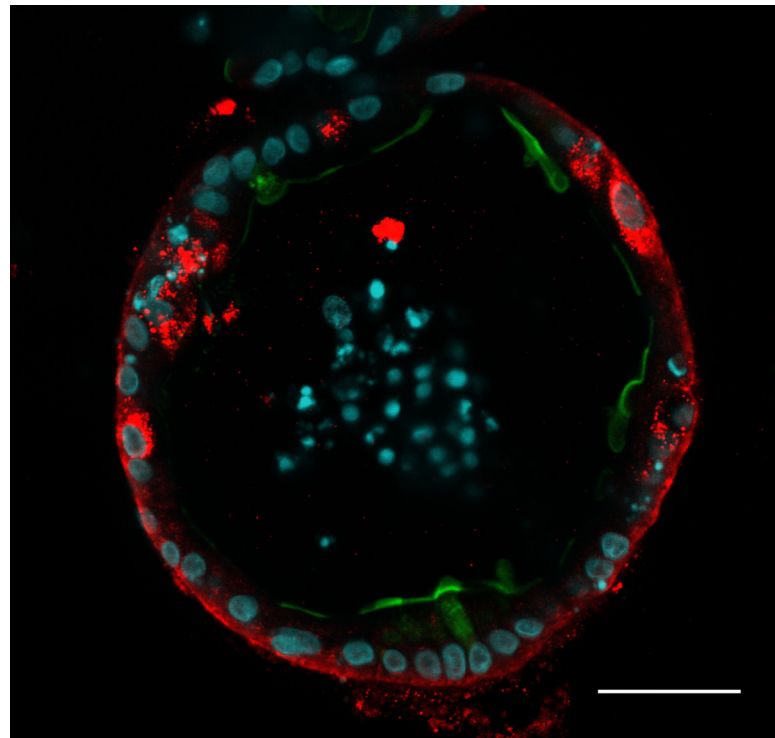
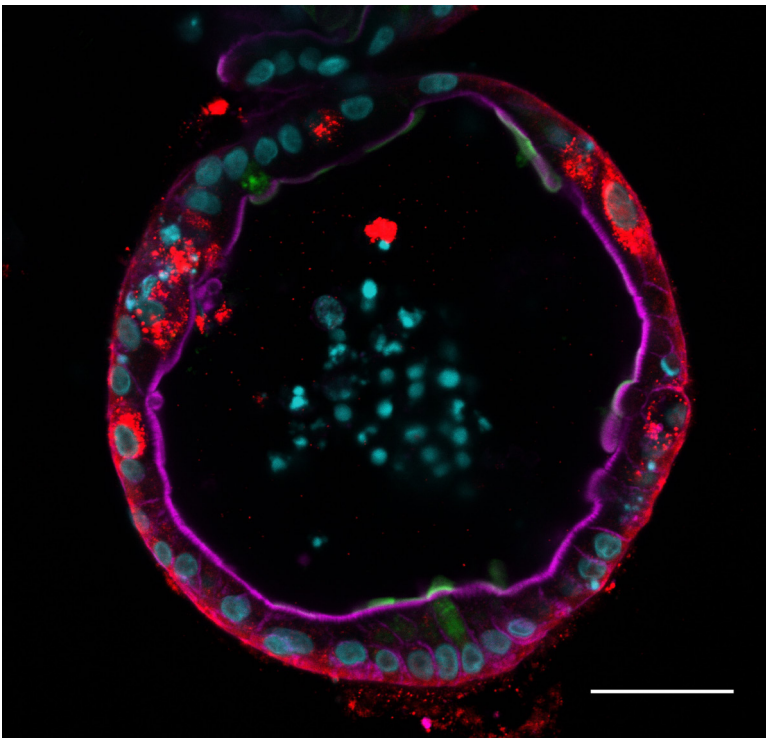
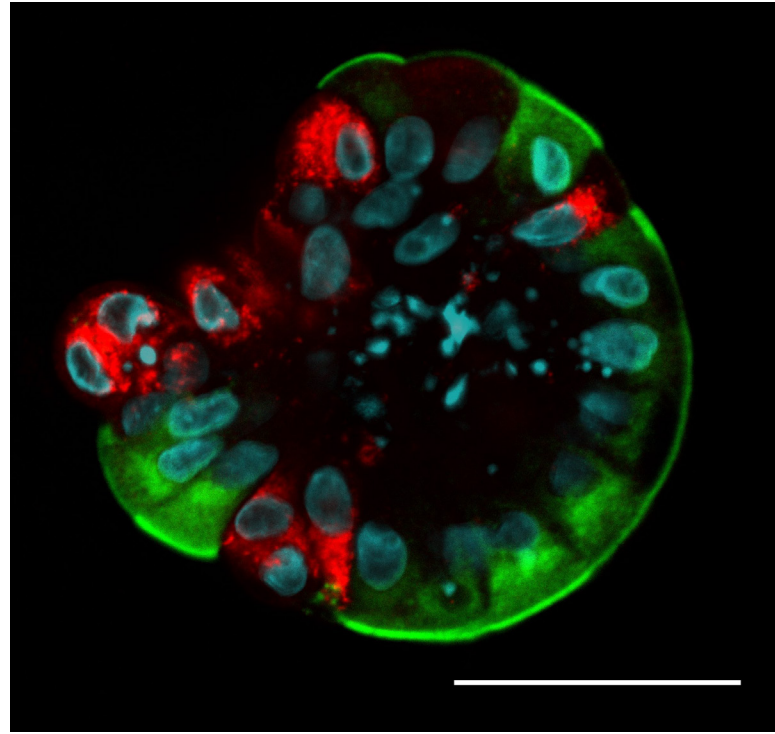
GGGAGAAGAACATGAAGATGATTGAAGTGCACAATCAGGAATGACAGGAAAGGAAACACAGCTTCACAATGGCCATGAACG

INDEL CONTRIBUTION SEQUENCE

+1 100% GTGAAGCTGTGTTTCCCTTCCCTGT; NATTCCTGATTGTGCAGTTCAATC

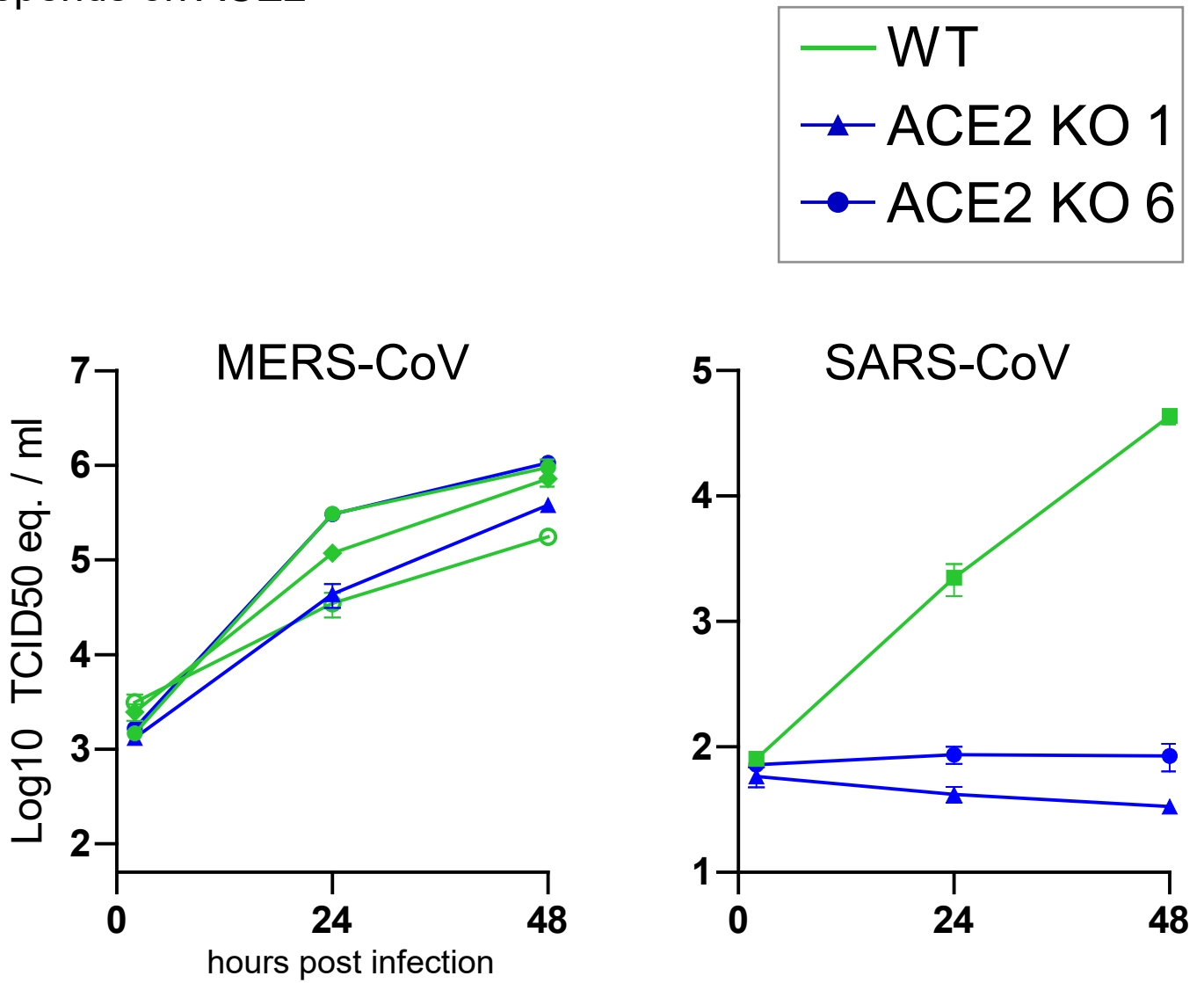
Supplementary figure 4 SARS-CoV-2 infected cells contain varying degrees of membranous ACE2 protein  
bioRxiv preprint doi: <https://doi.org/10.1101/2021.05.10.449531>; this version posted May 10, 2021. The copyright holder for this preprint (which was not certified by peer review) is the author/funder. All rights reserved. No reuse allowed without permission.

**ACE2** dsRNA (SARS-CoV-2) **Phalloidin** **DAPI**

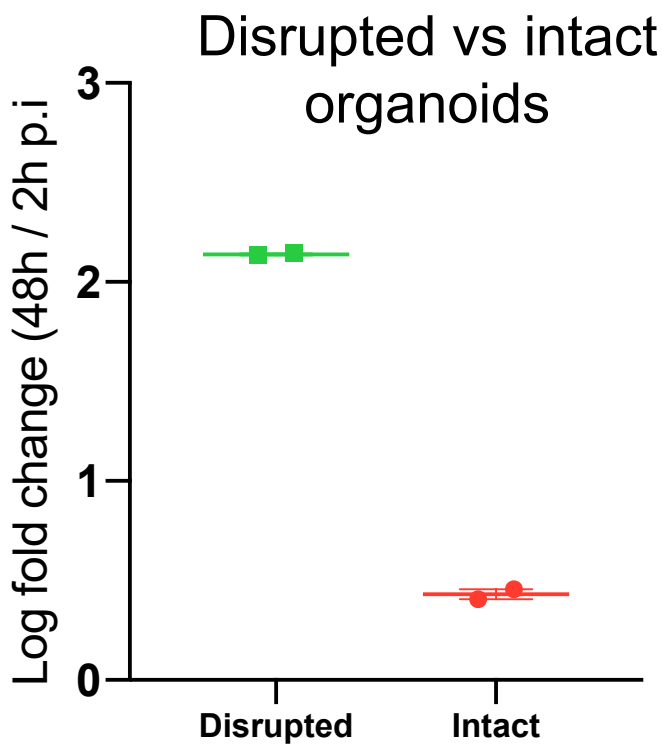


# Supplementary figure 5 SARS-CoV but not MERS-CoV replication depends on ACE2

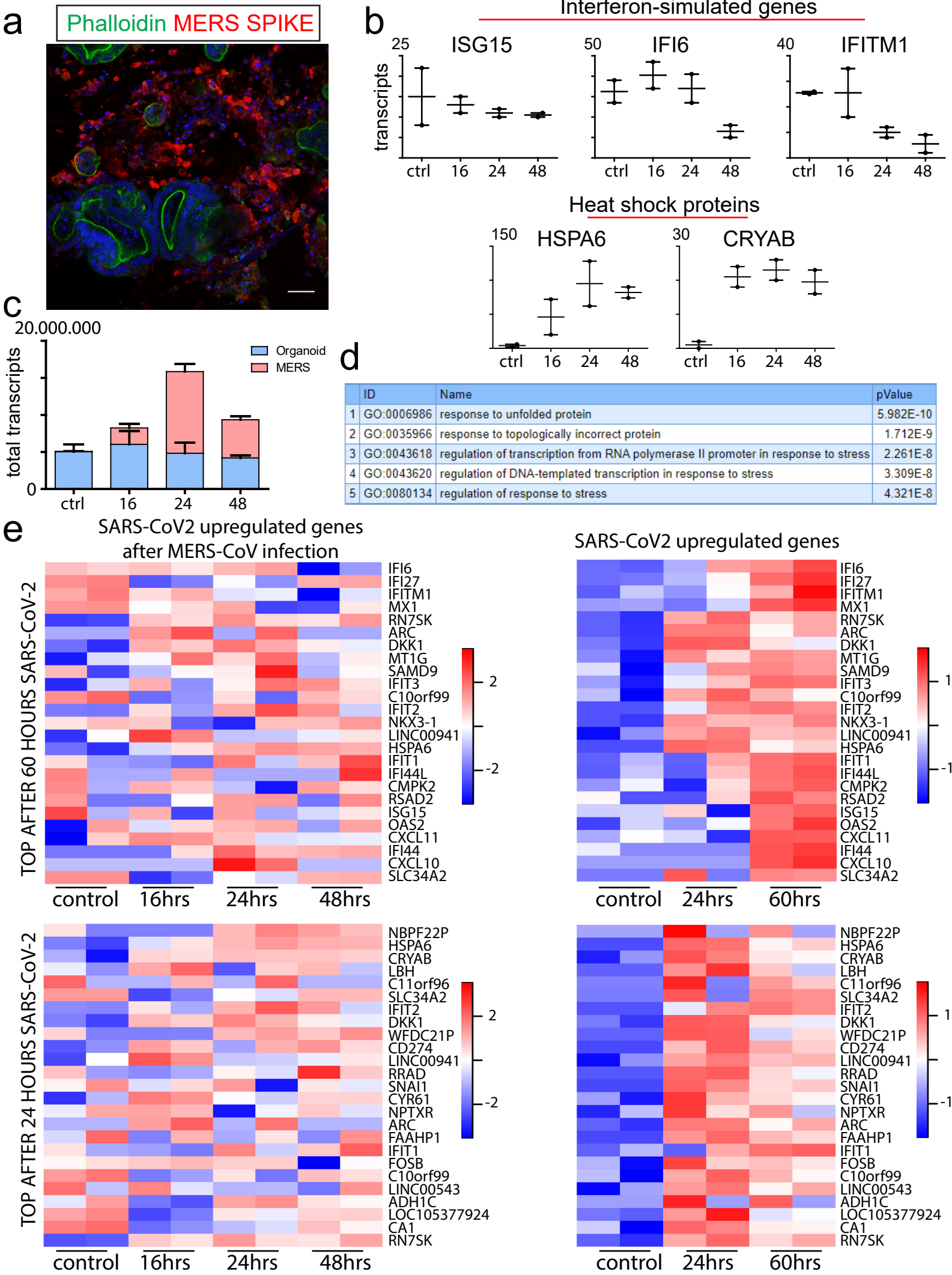
a



b

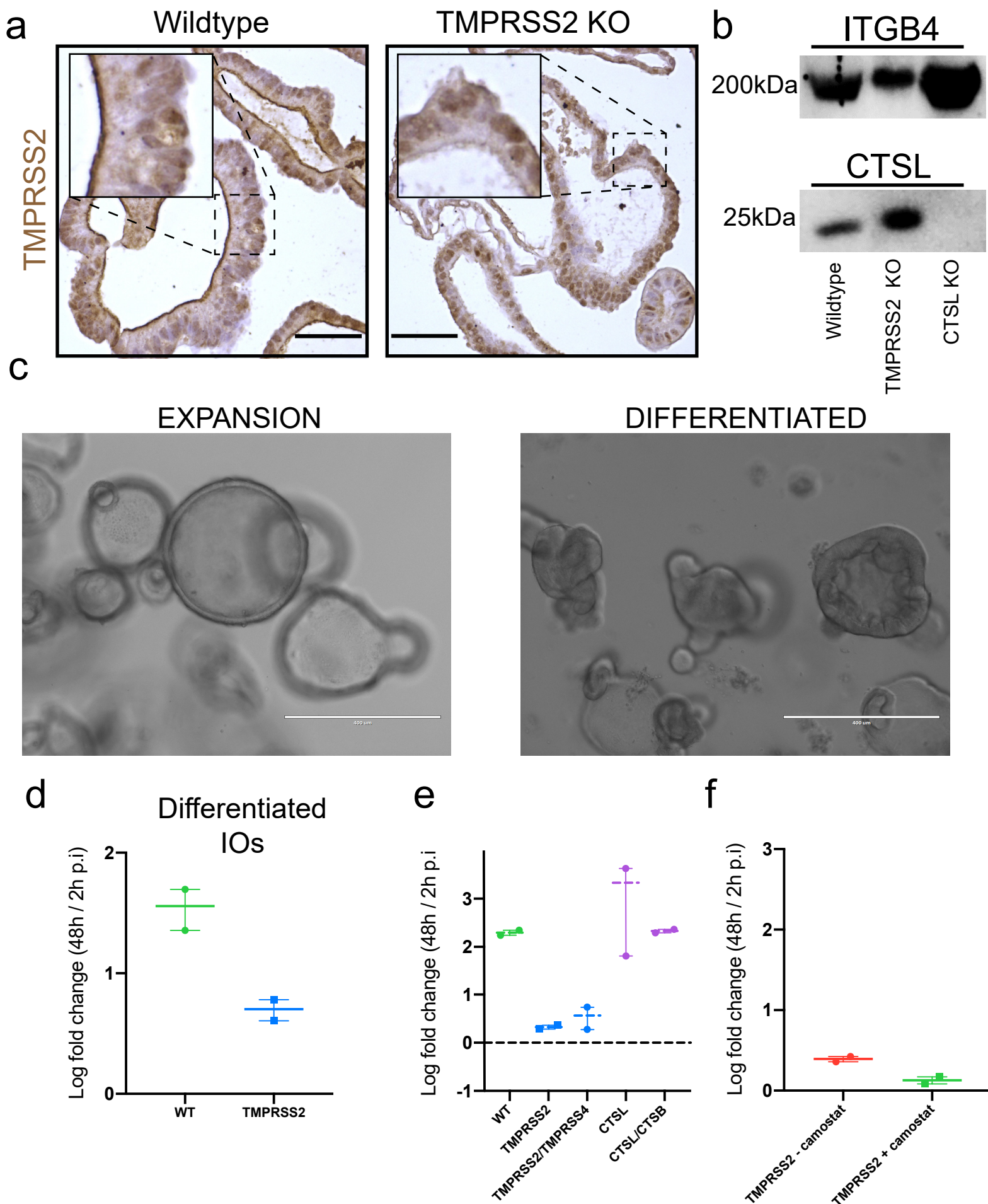


Supplementary figure 6 Establishment of MERS infection model in human intestinal organoids  
 (which was not certified by peer review) is the author/funder. All rights reserved. No reuse allowed without permission.





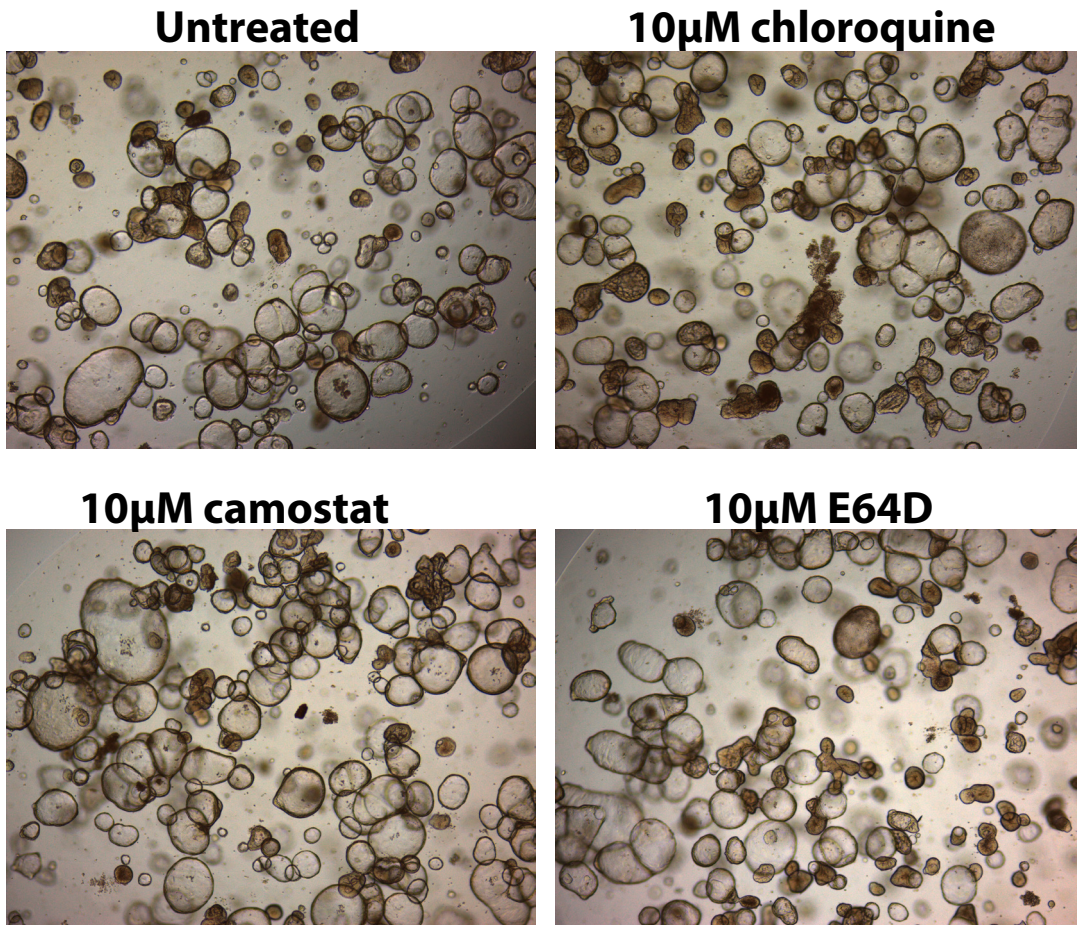
# Supplementary figure 7 Lack of redundancy in cathepsins and serine proteases in viral entry



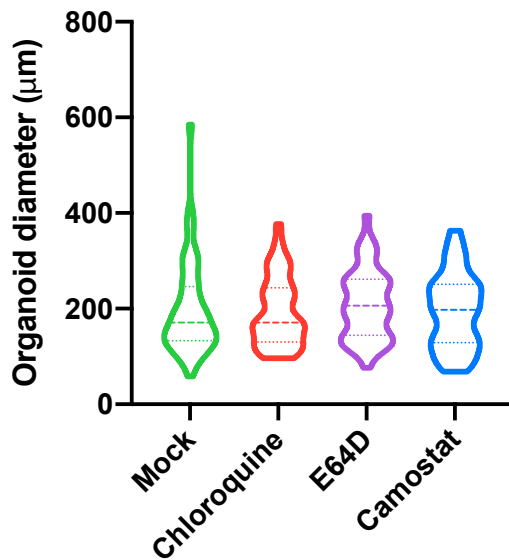
bioRxiv preprint doi: <https://doi.org/10.1101/2021.05.20.444952>; this version posted May 20, 2021. The copyright holder for this preprint (which was not certified by peer review) is the author/funder. All rights reserved. No reuse allowed without permission.

# Supplementary figure 8: Inhibition of serine proteases but not chloroquine inhibits viral replication in organoids

a



b



c

